In vivo susceptibility to energy failure parkinsonism and LRRK2 kinase activity

Salvatore Novello [a,*], Daniela Mercatelli [a,b], Federica Albanese [a], Chiara Domenicale [a], Alberto Brugnoli [a], Elisabetta D'Aversa [c], Silvia Vantaggiato [a], Sandra Dovero [d,e], Valentina Murtaj [f,g,i], Luca Presotto [f], Monica Borgatti [c], Derya R. Shimshek [h], Erwan Bezard [d,e], Rosa Maria Moresco [f,i,j], Sara Belloli [f,i,j], Michele Morari [a,*]

[a] Department of Neuroscience and Rehabilitation, University of Ferrara, 44121 Ferrara, Italy
[b] Technopole of Ferrara, LTTA Laboratory for Advanced Therapies, 44121 Ferrara, Italy
[c] Department of Life Science and Biotechnology, University of Ferrara, 44121 Ferrara, Italy
[d] Université de Bordeaux, Institut des Maladies Neurodégénératives, UMR 5293, F-33000 Bordeaux, France
[e] CNRS, Institut des Maladies Neurodégénératives, UMR 5293, F-33000 Bordeaux, France
[f] Nuclear Medicine Department, San Raffaele Scientific Institute, Milan, Italy
[g] PhD Program in Neuroscience, School of Medicine and Surgery, University of Milano Bicocca, Monza, Italy
[h] Department of Neuroscience, Novartis Institutes for BioMedical Research, Novartis Pharma AG, 4002 Basel, Switzerland
[i] Medicine and Surgery Department, University of Milano Bicocca, Monza, Italy
[j] Institute of Molecular Bioimaging and Physiology (IBFM), CNR, Segrate, Italy

ARTICLE INFO

ABSTRACT

The G2019S mutation of LRRK2 represents a risk factor for idiopathic Parkinson's disease. Here, we investigate whether LRRK2 kinase activity regulates susceptibility to the environmental toxin 1-methyl-4-phenyl-1,2,5,6-tetrahydropyridine (MPTP). G2019S knock-in mice (bearing enhanced kinase activity) showed greater nigro-striatal degeneration compared to LRRK2 knock-out, LRRK2 kinase-dead and wild-type mice following subacute MPTP treatment. LRRK2 kinase inhibitors PF-06447475 and MLi-2, tested under preventive or therapeutic treatments, protected against nigral dopamine cell loss in G2019S knock-in mice. MLi-2 also rescued striatal dopaminergic terminal degeneration in both G2019S knock-in and wild-type mice. Immunoblot analysis of LRRK2 Serine935 phosphorylation levels confirmed target engagement of LRRK2 inhibitors. However, MLi-2 abolished phospho-Serine935 levels in the striatum and midbrain of both wild-type and G2019S knock-in mice whereas PF-06447475 partly reduced phosphoSerine935 levels in the midbrain of both genotypes. *In vivo* and *ex vivo* uptake of the 18-kDa translocator protein (TSPO) ligand [^{18}F]-VC701 revealed a similar TSPO binding in MPTP-treated wild-type and G2019S knock-in mice which was consistent with an increased GFAP striatal expression as revealed by Real Time PCR. We conclude that LRRK2 G2019S, likely through enhanced kinase activity, confers greater susceptibility to mitochondrial toxin-induced parkinsonism. LRRK2 kinase inhibitors are neuroprotective in this model.

1. Introduction

Mutations in the leucine-rich repeat kinase 2 (*LRRK2*) gene are associated with a significant proportion of familial (5–6%) and idiopathic (1–2%) Parkinson's disease (iPD) (Healy et al., 2008). LRRK2-associated PD is clinically and neuropathologically indistinguishable from iPD (Kalia et al., 2015; Mestre et al., 2018), and shows autosomal dominant transmission with incomplete penetrance (Reed et al., 2019), suggesting an interplay among G2019S mutation, intrinsic (*e.g.* age) and environmental (*e.g.* toxins) factors. The c.6055G > A mutation, which results in a substitution of a glycine with a serine in position 2019 (p. G2019S) within the kinase domain, is most frequently associated with the disease (Correia Guedes et al., 2010; Reed et al., 2019). This mutation results in a higher kinase activity (Greggio et al., 2006; West et al., 2005; Yao et al., 2010), which is instrumental for *in vitro* (Greggio et al., 2006; Smith et al., 2006; West et al., 2007) and *in vivo* neurotoxicity (Lee et al., 2010; Xiong et al., 2018). On this basis, LRRK2 kinase inhibitors are being developed as disease-modifying agents (West, 2017) and are presently evaluated in clinical trials (Tolosa et al., 2020). MLi-2 (Scott et al., 2017), PF-06447475 (Fell et al., 2015) and PFE-360 (Fuji et al., 2015) are the most potent and selective brain-penetrant LRRK2 inhibitors developed so far, and their neuroprotective potential has been convincingly proven *in vitro*. Nonetheless, LRRK2 kinase inhibitors proved either effective (Daher et al., 2015; Nguyen et al., 2020; Rocha et al., 2020) or ineffective (Fell et al., 2015; Henderson et al., 2018; Kelly et al., 2021; Van der Perren et al., 2021) in attenuating nigro-striatal dopamine (DA) neuron degeneration in rodent models of PD. G2019S LRRK2 knock-in (G2019S KI) mice represent a suitable model to study the interplay between genetics, intrinsic and environmental factors in PD pathogenesis since they do not show overt nigro-striatal DA neuron degeneration (Volta and Melrose, 2017) but early signs of nigro-striatal dysfunction, affecting DA release (Tozzi et al., 2018; Yue et al., 2015), transport (Longo et al., 2017), and signaling (Migheli et al., 2013), as well as cortical glutamatergic transmission (Beccano-Kelly et al., 2014). Moreover, they show mitochondrial network disruption (Tozzi et al., 2018; Yue et al., 2015) and autophagy impairment (Schapansky et al., 2018; Wallings et al., 2019) accompanied by striatal and nigral accumulation of phosphoSerine 129 α-synuclein (α-syn), a possible toxic form of α-syn, most abundant in Lewy bodies (Oueslati, 2016), which might work to increase the susceptibility to PD triggers (Longo et al., 2017; Novello et al., 2018). Indeed, AAV human A53T α-syn overexpression caused larger synucleinopathy and nigro-striatal degeneration in G2019S KI mice compared to WT mice (Novello et al., 2018). To further confirm this view, we sought to investigate whether G2019S LRRK2 also confers higher susceptibility to the parkinsonian toxin 1-methyl-4-phenyl-1,2,5,6-tetrahydropyridine (MPTP), which selectively destroys dopaminergic neurons by blocking mitochondrial complex I and elevating oxidative stress (Betarbet et al., 2002; Schildknecht et al., 2017). Previous studies have reported larger nigro-striatal degeneration in BAC human G2019S transgenic mice exposed to acute MPTP (Arbez et al., 2020; Karuppagounder et al., 2016). Considering the confounders associated with this genetic model (overexpression of a human transgene in substantia nigra pars compacta, SNc, presence of endogenous murine LRRK2 simultaneously with human LRRK2 mutant), and the caveats of an acute protocol of MPTP administration, the contribution of LRRK2 kinase activity was studied in G2019S KI and wild-type (WT) mice subjected to subacute MPTP administration. As a comparison, mice with constitutive deletion of LRRK2 (KO mice) (Hinkle et al., 2012) and mice KI for the LRRK2 kinase-dead mutation D1994S (KD mice) (Herzig et al., 2011) were used. Furthermore, the neuroprotective effect of LRRK2 kinase inhibitors PF-06447475 and MLi-2 was investigated, and target engagement confirmed through immunoblot analysis of phosphoSerine935 (pSer935) LRRK2 (Deng et al., 2011; Dzamko et al., 2010) and phosphoThreonine73 (pThr73) Rab10 (pRab10) (Ito et al., 2016; Thirstrup et al., 2017) levels, as readout of LRRK2 kinase activity. To collect preliminary information on the neuroprotective mechanisms

underlying the action of LRRK2 inhibitors, microgliosis and astrogliosis were evaluated through immunohistochemistry of ionized calcium binding adaptor molecule 1 (iba-1) and glial fibrillary acid protein (GFAP; astrocyte marker). The impact of MPTP on neuroinflammation markers was also investigated by *in vivo* and *ex vivo* computed tomography/positron emission tomography (CT/PET) imaging with the 18-kDa translocator protein (TSPO) ligand, [^{18}F]-VC701 (Di Grigoli et al., 2015), coupled to expression analysis (qRT-PCR) of striatal TSPO, transmembrane protein 119 (TMEM119, microglia marker), GFAP, inducible nitric oxidase synthase (iNOS) and cyclooxygenase 2 (COX-2) (pro-inflammatory genes) and Arginase 1 (Arg1) (anti-inflammatory gene).

2. Materials and methods

2.1. Animals

Experimental procedures involving the use of animals complied with the ARRIVE guidelines and the EU Directive 2010/63/EU for animal experiments and were approved by the Ethical Committees of the University of Ferrara and San Raffaele Hospital (Milano), and the Italian Ministry of Health (license 102/2017-PR). Three to four-month-old, male homozygous G2019S KI, LRRK2 KO, KD mice, and age-matched WT controls, backcrossed on a C57BL/6 J background, were used (Albanese et al., 2021; Longo et al., 2017; Longo et al., 2014; Mercatelli et al., 2019). Founders were obtained from Novartis Pharma (G2019S KI and KD mice) (Herzig et al., 2011) and from Mayo Clinic (Jacksonville, FL, USA) (LRRK2 KO mice) (Hinkle et al., 2012). Mice were kept under regular lighting conditions (12 h light/dark cycle), with free access to food (4RF21 standard diet; Mucedola, Settimo Milanese, Milan, Italy) and water. Animals were housed in groups of 5 for a 55x33x20 cm polycarbonate cage (Tecniplast, Buguggiate, Varese, Italy) with a Scobis Uno bedding (Mucedola, Settimo Milanese, Milan, Italy) and environmental enrichments.

2.2. Experimental design

In the first experiment, four cohorts of 3-month-old G2019S KI (n = 22), LRRK2 KO (n = 16), KD (n = 16) and WT (n = 22) male mice (n = 18–22 each) were randomly divided in two balanced groups and treated with MPTP 30 mg/Kg (i.p.) or saline once daily for 7 days. Twenty-four hours after the end of treatment, animals were anaesthetized with isoflurane, transcardially perfused with 4% paraformaldehyde (PFA), and brains extracted and processed for tyrosine hydroxylase (TH) immunohistochemistry. Two different protocols were adopted to assess the neuroprotective potential of LRRK2 inhibitors (Supplementary Fig. 1). In the first one, 32 3-month-old mice were pretreated with PF-06447475 (10 mg/kg twice daily, i.p.) or vehicle (n = 16 each) for 3 days, then each cohort was split into two subgroups receiving either PF-06447475 + MPTP or PF-06447475 alone, MPTP or saline for further 7 days. In the second protocol, a "clinically-relevant" approach was adopted since PF-06447475 was given therapeutically after the onset of MPTP treatment. Twenty-four G2019S KI mice were allotted in 3 groups (n = 8/group) and treated with vehicle for 14 days, MPTP for 7 days followed by saline for 7 days, or the combination of MPTP and PF-06447475 (for 10 days, starting from the 4th day after MPTP). A control group treated with PF-06447475 alone was not included in this experiment since, as shown in Fig. 3, PF-06447475 alone did not affect the number of nigral DA cells. The protocol used in G2019S KI mice was replicated in a balanced cohort of 24 WT mice (n = 8/group). A "clinically driven" protocol was also adopted to investigate the neuroprotective properties of MLi-2 (10 mg/kg i.p. twice daily). Two cohorts of G2019S KI and WT mice (n = 36 each) were divided into four balanced groups and administered with saline, MPTP, MLi-2 alone, or in combination with MPTP. Finally, to prove the selectivity of MLi-2, this protocol was replicated in 24 LRRK2 KO mice treated with MPTP, MPTP + MLi-2 and vehicle (n = 8 each).

Target validation was performed in 18 WT and 18 G2019S KI 3–4 month-old male mice. Each cohort was divided in three groups (n = 6 each) randomly receiving PF-06447475 or MLi-2 (both at 10 mg/Kg i.p. twice daily), or an equivalent amount of vehicle for 10 days. General health conditions along with weight, mobility, tremor, hind-limb clasping, body condition, coat and eyes appearance were assessed and scored before each first daily injection. At the end of treatment, two hours after the last injection, mice were anaesthetized and euthanized *via* cervical dislocation. Brains were extracted, the striatum and midbrain excised and processed for Western blot analysis of pSer935 LRRK2 and pRab10.

For imaging studies, 3–4-month-old male G2019S KI mice WT controls (n = 30 each group) were recruited. For *in vivo* study, 8 G2019S KI and 6 WT mice underwent the first CT and PET [^{18}F]VC701 acquisitions before starting MPTP treatment (as above) (d0) and the second CT and PET acquisitions at the end of the 7 day-treatment (d7). For *ex vivo* biodistribution analysis of [^{18}F]VC701, 10 G2019S KI and 9 WT mice were treated with MPTP, and 10 G2019S KI and 9 WT mice with vehicle.

2.3. Immunohistochemistry

Immunohistochemistry was performed as previously described (Longo et al., 2017; Novello et al., 2018). Briefly, 50 μm-thick free-floating sections of the striatum (AP from +1.0 to −1.25 from bregma) and the SNc (AP from −3.16 to −3.52 from bregma (Paxinos and Franklin, 2001) were tested for a rabbit polyclonal antibody raised against TH (ab112; 1:750 in BSA 1% PBST; Abcam, Cambridge, UK), iba-1 (ab178846; 1:2000 in BSA 1% PBST; Abcam, Cambridge, UK) or GFAP (G9269, 1:100 in BSA 1% PBST, Merck Millipore, Darmstadt, Germany). Sections were then rinsed and incubated for 1 h with an anti-rabbit HRP-conjugated secondary antibody (ab6721, 1:500 in BSA 1% PBST; Abcam, Cambridge UK) and revealed by a DAB substrate kit (ab64238, Abcam, Cambridge, UK). Sections were mounted on gelatinized slides, dehydrated, and coverslipped for further analysis.

2.4. Stereological counting

Stereological analysis was performed by counting TH+ neurons (phenotypic marker) and cresyl violet stained cells (structural marker) in SNc, according to an unbiased stereological sampling method based on optical fractionator stereological probe, as previously described (Longo et al., 2017; Novello et al., 2018). A Leica DM6B motorized microscope (Leica Microsystems, Milan, Italy) coupled with a Stereo Investigator software (MBF Europe, Delft, The Netherlands) was used. Counting was performed on 5 consecutive 50 μm-thick slices, magnified at 63 × .

2.5. TH quantification in the striatum

Images were taken at 2.5× or 10× magnification with a Leica DM6B motorized microscope, and optical densitometry analyzed off-line as grey level with ImageJ using the corpus callosum as background (Novello et al., 2018).

2.6. Iba-1 and GFAP analysis

Three consecutives sections were mounted on a coverslip and images were obtained using a Leica DM6B motorized microscope, and later analyzed with ImageJ software (Novello et al., 2018). Iba-1+ cells were binarized and number of cells, circularity and area of surface occupied in pixels^2 were quantified to compare the different treatments. For GFAP analysis, striatum limits were delineated to obtain a representative surface of protein expression. Finally, the immunopositive surface was calculated as percentage of total striatum area.

2.7. Western blot

Western blot analysis was performed as previously described (Longo et al., 2017; Mercatelli et al., 2019). Briefly, 30 μg of protein obtained from striatal and midbrain homogenates were loaded onto 4% to 12% gradient polyacrilamide precast gels (Bolt 4%–12% Bis-Tris Plus Gels; Life Technologies, Carlsbad, CA, USA) and transferred onto polyvinyl difluoride membrane, blocked for 60 min with 5% nonfat dry milk in 0.1% Tween 20 Tris-buffered saline, and incubated overnight at 4 °C with rabbit anti-pSer935 LRRK2 antibody (ab133450, 1:500, Abcam, Cambridge, UK) or pThr73 Rab10 (ab230261, 1:1000, Abcam, Cambridge, UK). Midbrain homogenates were also probed for TH with anti-rabbit TH antibody (ab112, 1:600, Abcam, Cambridge, UK). Horseradish peroxidase-linked secondary antibody (goat anti-rabbit IgG HRP-conjugate 12–348, 1:4000, Merck Millipore, Darmstadt, Germany) was used and immunoreactive proteins were visualized by enhanced chemiluminescence (ECL) detection kit (Pierce™ BCA Protein Assay Kit, Thermo Scientific or ECL+, GE Healthcare). Images were acquired and quantified using the ChemiDoc MP System and the ImageLab Software (Bio-Rad). Membranes were then stripped and re-probed with rabbit anti-LRRK2 (ab133474, 1:1000, Abcam, Cambridge, UK) or rabbit anti-GAPDH antibody (ABS16, 1:1000, Merck Millipore, Darmstadt, Germany). Data were analyzed by densitometry; the optical density of pSer935 LRRK2 was normalized to total LRRK2 whereas total LRRK2 and pThr73 Rab10 were normalized to GAPDH levels. To minimize experimental variability, each blot was replicated twice, and data averaged.

2.8. qRT-PCR

Total RNA was isolated using TRI Reagent (Sigma-Aldrich, Saint Louis, Missouri, USA) following the manufacturer's instructions, washed once with cold 75% ethanol, dried and resuspended in 10 μl of RNAse free water. Final RNA concentration was determined using SmartSpec Plus spectrophotometer (Bio-Rad, Hercules, California, USA) and then stored at −80 °C until use. A total amount of 1 μg of RNA was reverse transcribed to cDNA, after DNAse treatment, using the iScript gDNA Clear cDNA Synthesis Kit (Bio-Rad), incubating it for 5 min at 25 °C, 20 min at 46 °C and 1 min at 95 °C, in a final reaction volume of 20 μl. For real-time qPCR analysis, 1.8 μl of cDNA was used for each reaction to quantify the relative gene expression. cDNA was amplified with iQ SYBR Green Supermix (Bio-Rad) in a 20 μl reaction using the CFX96 Touch Real-Time PCR Detection System (Bio-Rad): after an initial denaturation at 95 °C for 3 min, the reactions were performed for 40 cycles (each cycle consisting in 15 s at 95 °C and 1 min at 60 °C). To perform the PCR reaction, primers for TSPO, TMEM-119, iNOS, COX2, Arg1, GFAP, β-actin, and HPRT (sequences reported in Supplementary Table 1) were purchased from Invitrogen (Thermo Fischer Scientific, Carlsbad, California, USA). Each target gene expression was normalized with the mean of the expression of housekeeping genes (β-actin and HPRT), and the relative quantification was calculated using the ΔΔCt method.

2.9. Imaging studies

2.9.1. In vivo CT/PET study with [^{18}F]-VC701

The radiotracer [^{18}F]-VC701 was prepared as described (Di Grigoli et al., 2015). CT and PET acquisitions were performed using X-cube® and β-cube® (Molecubes, Gent, BE), respectively. On the day of CT/PET imaging, animals were injected in a tail vein with 4.67 ± 0.3 MBq of radiotracer and maintained under a red warm lamp. After about 90 min for tracer uptake, each animal was anaesthetized with 2% isoflurane in medical air and then positioned prone on the scanner bed for the CT scan centered on the brain (exam duration: 4 min, X-Ray beam duration: 90 s, kVp: 40, current: 400 μA, rotation time: 60 s, angular views: 960). At the end of the CT acquisition, the bed with the immobilized animal was removed and inserted in the PET scanner for a 20 min static acquisition.

PET scan was started 100 min after injection. During the exam, mice were maintained under anesthesia, and body temperature and respiratory rate were constantly monitored.

2.9.2. CT/PET images analysis

CT and PET data were reconstructed using the proprietary Molecubes software included in the system. CT images were reconstructed with a 200 μm isotropic pixel size using a standard ISRA algorithm. PET images were reconstructed using a List-Mode OSEM algorithm with 30 iterations and 400 μm isotropic voxel size, accounting for the tracer decay correction. Thanks to the bed positioning system, PET and CT images are automatically co-registered.

CT/PET images were processed using Region of Interest (ROI) analysis and Statistical Parametric Mapping (SPM). SPM is a voxel-based operator-independent analysis that allows the identification of brain regions resulting above a statistical threshold in between groups or conditions comparisons. The program was adapted in our laboratory for small animal use and tested as a potential tool to detect group or condition effect on neuroinflammation. In detail, ROI analysis was performed using PMOD software 4.1 (Zurich, Switzerland) where the high-resolution CT images were manually co-registered to an MRI brain template (Ma et al., 2005). The estimated transformation was applied to the PET image. After realignment to this standard space, ROIs from the atlas were applied to the PET image to extract activity values. SN ROI was manually drawn as the brain template does not include it. Radioactivity values were calculated as standard uptake values (SUV) obtained as follows: after image calibration in MBq/cc using a calibration phantom, radioactivity concentration in each brain voxel is corrected for [^{18}F]-decay ($T_{1/2}$ = 109.8 min) from brain counting to the time of radiopharmaceutical injection. Radioactivity concentration in the brain is then divided for the injected dose and multiplied for animal weight. SUV is the standard index of radiopharmaceutical uptake used either in preclinical and clinical research. For SPM, a CT image was generated by manual registration and averaging multiple animals between themselves using SPM tools (SPM 12, http://www.fil.ion.ucl.ac.uk/spm/software/spm12/). The final image was rigidly co-registered to the same MRI template used for the manual analysis. For the analysis phase, each CT was non-linearly wrapped in this new space using the SPM normalization algorithm (Ashburner and Friston, 1999). The estimated transformation was applied to the corresponding PET scan. To reduce inter-subject variability, and due to the lack of a potential reference region where no inflammatory response can be defined *a priori*, image intensity was scaled to the global mean uptake of the brain. Isotropic smoothing with a 1.7 mm FWHM Gaussian kernel was applied.

2.9.3. Ex vivo study with [^{18}F]-VC701

At the end of MPTP treatment, mice were injected with [^{18}F]-VC701 (4.46 ± 0.4 MBq) in a tail vein and maintained under a red warm lamp for tracer uptake. After 120 min, mice were anaesthetized with 4% isoflurane in medical air and euthanized by decapitation. Blood samples were obtained from retro-orbital collection. A sample of blood (100 μl) was transferred into a tube, while the remaining was centrifuged to obtain plasma for the radioactivity counting. Brain was rapidly removed, rinsed into cold heparinized PBS, and divided into different brain regions, including anterior and posterior cortex, striatum, SN, hippocampus and cerebellum, which were placed into pre-weighed tubes. All tubes were counted in a gamma-counter (LKB Compugamma CS1282, Wallac). After counting, tissue and blood/plasma radioactivity concentration were corrected for radioisotope decay and expressed as SUV, as previously described for PET, with the exception that radioactivity concentration was measured using a gamma counter.

2.10. Statistical analysis

Data are expressed as absolute values and are mean ± SEM of n mice. Statistical analysis was performed using Prism 8.0 (GraphPad Software

Inc., CA, USA). $P < 0.05$ values were considered statistically significant. Drug effect was analyzed by one-way, two-way or three-way ANOVA followed by the Tukey test for multiple comparisons. A two-tailed Student *t*-test was used to compare two groups of unpaired data. *In vivo* CT/PET comparison between groups was performed in the same subjects (pre- and post-MPTP) using a two-tailed Student t-test for paired data (test re-test). Imaging ROI data are expressed as SUV and presented as mean ± SEM of n mice. SPM analysis was performed at the voxel level. Clusters of statistically significant voxels were defined using a threshold of $p < 0.01$ and a minimum cluster extent of 50 voxels, without corrections for multiple comparisons. *Ex vivo* biodistribution analysis was performed using two-way ANOVA followed by the Tukey test for multiple comparisons.

2.11. Drugs

MPTP, PF-06447475, and MLi-2 were purchased from Carbosynth (Compton, Berkshire, UK). MPTP was dissolved in saline. PF-06447475 and MLi-2 were dissolved in 2% DMSO and 30% hydroxypropyl β-cyclodextrin. The radiotracer [^{18}F]-VC701 was prepared as described (Di Grigoli et al., 2015) and dissolved in saline before injection.

3. Results

3.1. MPTP caused larger nigro-striatal toxicity in G2019S KI mice compared to WT, LRRK2 KO and KD mice

To confirm the greater susceptibility of G2019S KI mice to MPTP, the toxin was administered subacutely to WT, LRRK2 KO, KD and G2019S KI mice for 7 days, and the integrity of the nigro-striatal pathway was investigated 24 h after the end of treatment (Fig. 1, Supplementary Fig. 1). Two-way ANOVA revealed that MPTP caused the loss of TH+ neurons in the SNc of all genotypes (treatment $F_{1,67}$ = 447.70, $p <$ 0.0001) (Fig. 1A). The reduction of TH+ neurons was similar in WT, LRRK2 KO, and KD mice (50%) but significantly greater in G2019S KI mice (75%) (treatment X genotype $F_{3,67}$ = 7.00, $p = 0.0004$) (Fig. 1A). Consistently, MPTP reduced the density of striatal TH+ terminals in all genotypes (treatment $F_{1,54}$ = 363.2, $p < 0.0001$) and G2019S KI mice showed a larger reduction (-80%) compared to WT, LRRK2 KO, and KD mice ($-45-60\%$; Fig. 1B) (treatment X genotype $F_{3,54}$ = 8.53, $p <$ 0.0001).

3.2. LRRK2 inhibitors protected from MPTP-induced neurotoxicity

To investigate the neuroprotective potential of LRRK2 inhibitors, the ability of PF-06447475 (10 mg/Kg, twice daily i.p.) (Henderson et al., 2015) to preserve the TH phenotype in G2019S KI mice was first investigated (Supplementary Fig. 1). MPTP caused a 72% reduction of TH+ neurons, which was prevented by PF-06447475 (MPTP X PF-06447475 interaction $F_{1,24}$ = 45.97, $p < 0.0001$) (Fig. 2A). MPTP also caused a similar 75% loss of TH+ terminals in the striatum but, quite surprisingly, PF-06447475 failed to affect it ($F_{1,28}$ = 0.02, $p = 0.87$) (Fig. 2B). PF-06447475 was then administered to G2019S KI and WT mice 4 days after the onset of MPTP treatment, according to a "clinically-relevant" protocol (Fig. 3; Supplementary Fig. 1). Two-way ANOVA revealed a significant effect of treatment ($F_{2,42}$ = 99.18 $p < 0.0001$), genotype ($F_{1,42}$ = 14.78 $p = 0.0004$) and genotype X treatment interaction ($F_{2,42}$ = 6.56 $p = 0.0033$). Again, MPTP caused a larger DA neuron degeneration in G2019S KI mice (70%) than WT mice (43%) (Fig. 3A). PF-06447475 did not affect the MPTP-induced loss of nigral DA neurons in WT mice but attenuated the excessive loss seen in G2019S KI mice, bringing the number of spared neurons close to that observed in WT animals (Fig. 3A). Different from SNc, PF-06447475 was again unable to affect the MPTP-induced striatal TH+ terminal degeneration in both genotypes (Fig. 3B) (treatment $F_{2,42}$ = 275.51 $p < 0.0001$, genotype $F_{1,42}$ = 0.89 $p = 0.34$, genotype X treatment interaction $F_{2,42}$ = 0.08
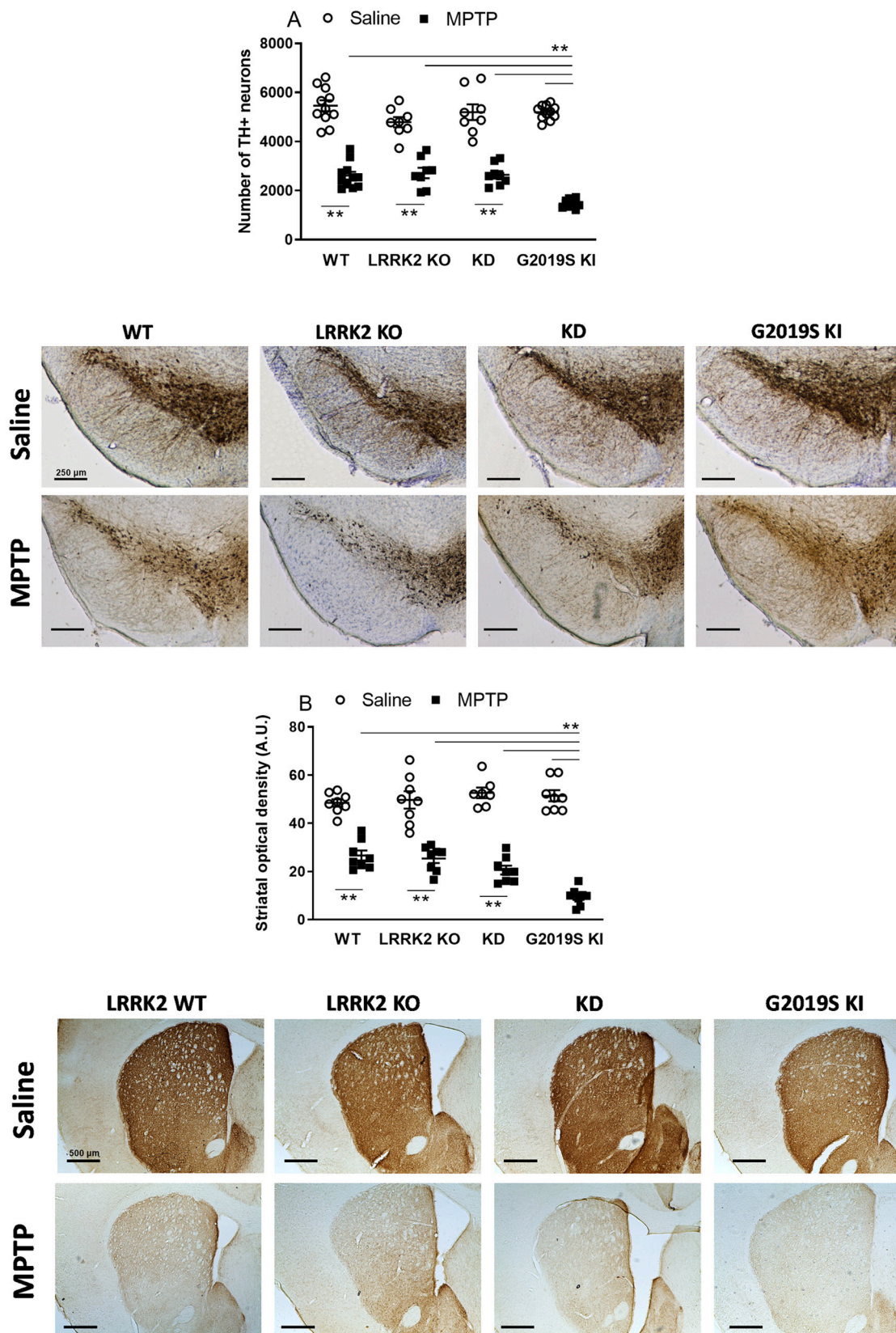
Fig. 1. Degeneration of dopamine (DA) neurons in the substantia nigra compacta (SNc) and tyrosine hydroxylase (TH) positive terminals in the striatum of G2019S KI, LRRK2 KO, KD and WT mice following subacute treatment with MPTP. Mice were treated with MPTP (30 mg/Kg i.p. once daily for 7 days), then euthanized 24 h after the last injection. A. Stereological quantification of DA neurons in SNc, and representative images (scale bar = 250 μm). B. Quantification of optical density (greyscale arbitrary units) in striatal slices, and representative images (scale bar = 500 μm). Data represent individual values (8 mice/group in the WT and G2019S KI cohorts, and 8 mice/group in the LRRK2 KO and KD cohorts), with means ± SEM. **p < 0.01 according to two-way ANOVA followed by the Tukey test for multiple comparisons.
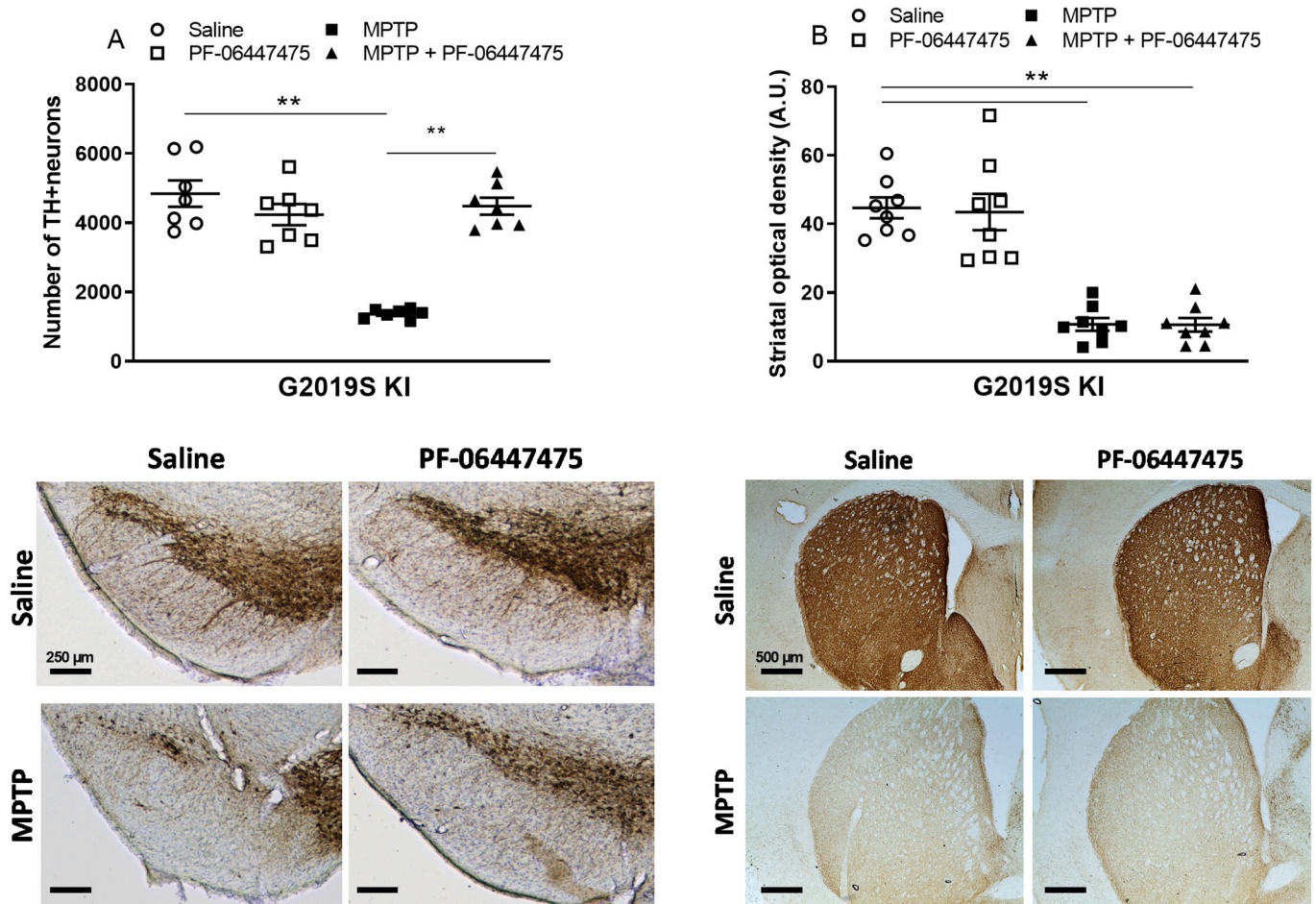
Fig. 2. Effect of prophylactic treatment with the LRRK2 inhibitor PF-06447475 on MPTP-induced dopaminergic nigro-striatal tract degeneration in G2019S KI mice. Mice were pre-treated with PF-06447475 (10 mg/Kg i.p. twice daily), then administered subacute MPTP (30 mg/Kg, i.p. once daily) for 7 days. Mice were euthanized 24 h after the last MPTP injection. Stereological quantification of tyrosine hydroxylase (TH) positive DA neurons in substantia nigra compacta (A) and optical density of TH positive terminals in the striatum (B), along with representative images. Scale bar = 250 μm (A) or 500 μm (B). Data are expressed as the number of TH positive neurons (A) and striatal optical density (greyscale arbitrary units, B), and represent individual values (7 mice/group), with means ± SEM. **p < 0.01 according to two-way ANOVA followed by the Tukey test for multiple comparisons.

p = 0.92), as observed in the prophylactic treatment mode (Fig. 2B). To confirm the neuroprotective potential of LRRK2 inhibitors, MLi-2 was also tested under a "clinically-relevant" therapeutic protocol (Figs. 4-5; Supplementary Fig. 1). Three-way ANOVA revealed an overall effect of genotype ($F_{1,64}$ = 9.71 p = 0.0027), MPTP ($F_{1,64}$ = 217.0 p < 0.0001) and MLi-2 ($F_{1,64}$ = 6.42, p = 0.0137). Expectedly, MPTP again caused a larger degeneration of DA neurons in G201S KI mice (66%) compared to WT mice (35%) (genotype X MPTP $F_{1,64}$ = 6.61 p = 0.0124) (Fig. 4). MLi-2, ineffective on its own, attenuated the excessive loss of DA neurons in G2019S KI but had no effect in WT mice (genotype X MPTP X MLi-2) ($F_{1,64}$ = 6.92 p = 0.0107). Three-way ANOVA on striatal data (Fig. 5) revealed an overall MPTP effect ($F_{1,64}$ = 109.0, p < 0.0001) and MLi-2 ($F_{1,64}$ = 85.6, p < 0.0001) but not genotype ($F_{1,64}$ = 3.48 p = 0.0667). MPTP again caused a more profound loss of TH+ terminals in the striatum of G2019S KI mice with respect to WT controls (genotype X MPTP $F_{1,64}$ = 109.0 p < 0.0001) (Fig. 5) and MLi-2 rescued this loss in both genotypes ($F_{1,64}$ = 4.51 p = 0.0376). To confirm that the neuroprotective effect of MLi-2 was not due to off-targets, MLi-2 was administered to LRRK2 KO mice treated with MPTP (Fig. 6). MPTP caused a similar reduction of the number of nigral DA neurons ($F_{2,21}$ = 89.84 p < 0.0001; Fig. 6A) and striatal TH+ terminals ($F_{2,21}$ = 17.22 p < 0.0001; Fig. 6B) in mice treated with saline or MLi-2, indicating that MLi-2 was ineffective in the absence of LRRK2.

3.3. Analyses of PF-06447475 and MLi-2 LRRK2 engagement in vivo

To prove target engagement of kinase inhibitors, PF-06447475 and MLi-2 were administered to WT and G29019S KI mice at the same dosage used in the treatment protocol (10 mg/kg i.p. twice daily for 10 days) and levels of pSer935 LRRK2 and pRab10 measured in striatal and midbrain homogenates by immunoblot analysis. LRRK2 inhibitors did not affect general mouse health conditions or mouse weight (Supplementary Fig. 2) indicating that PF-06447475 and MLi-2 were well tolerated at the dosage used. Two-way ANOVA on striatal pSer935 LRRK2 levels (expressed as a ratio to total LRRK2 levels, Fig. 7A) revealed a significant effect of treatment ($F_{2,30}$ = 39.98, p < 0.0001). PF-06447475 was ineffective in WT mice and G2019S KI mice, but the unexpected high variability observed in WT mice confounded statistical analyses. MLi-2 on the other hand almost abolished pSer935 levels in both genotypes. Statistical analysis on striatal LRRK2 levels (Fig. 7B) revealed a significant effect of genotype ($F_{1,30}$ = 62.27, p < 0.0001), confirming our previous finding (Mercatelli et al., 2019) that LRRK2 levels were 40% lower in G2019S KI mice with respect to WT mice. Two-way ANOVA on midbrain pSer935 LRRK2 levels (Fig. 7C) revealed a significant effect of treatment ($F_{2,30}$ = 91.17, p < 0.0001). PF-06447475 significantly reduced pSer935 levels by 50% in WT mice and by 30% in G2019S KI mice whereas MLi-2 almost abolished pSer935 in both genotypes. As in striatum, a significant reduction (35% overall) of LRRK2
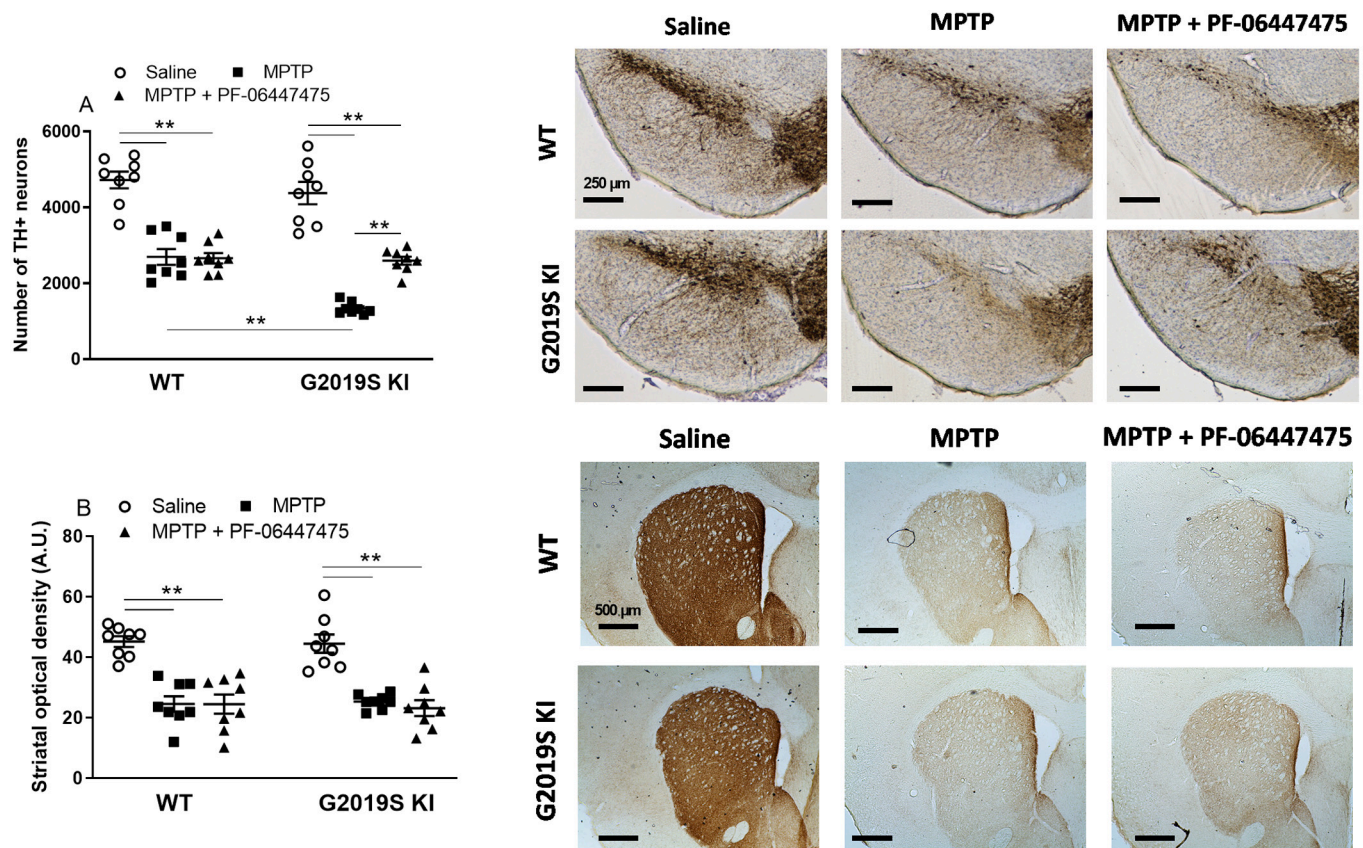
Fig. 3. Effect of therapeutic treatment with the LRRK2 inhibitor PF-06447475 on MPTP-induced dopaminergic nigro-striatal tract degeneration in G2019S KI and WT mice. Mice were administered subacute MPTP (30 mg/Kg, i.p. once daily for 7 days) and, starting from the 4th day onwards, also with PF-06447475 (10 mg/Kg i.p. twice daily) for 10 days. Mice were euthanized 24 h after the last PF-06447475 injection. Stereological quantification of tyrosine hydroxylase (TH) positive dopamine (DA) neurons in SNc (A) and optical density of TH positive terminals in the striatum (B), along with representative images. Scale bar = 250 μm (A) or 500 μm (B). Data are expressed as the number of TH positive neurons (A) and striatal optical density (greyscale arbitrary units, B) and represent individual values (8 mice/group), with means ± SEM. **p < 0.01 according to two-way ANOVA followed by the Tukey test for multiple comparisons.

levels was observed in the midbrain of G2019S KI mice (genotype effect $F_{1,28} = 19.43$ p $= 0.0001$; Fig. 7D). Neither inhibitor reduced total LRRK2 levels. To confirm correct midbrain sampling, immunoblot analysis on TH levels was performed (Supplementary Fig. 3): two samples were discarded due to faint TH signal. Finally, pRab10 levels were also measured. Different from pSer935, however, pRab10 levels in striatal and midbrain homogenates were not affected by LRRK2 inhibitors (Supplementary Fig. 4).

3.4. MPTP modulates [18F]-VC701 uptake

To test PET feasibility of providing insights into the mechanism underlying the increased susceptibility of G2019S KI mice to MPTP, the neuroinflammatory response was monitored *in vivo* and *ex vivo* using the TSPO ligand [^{18}F]-VC701 (Belloli et al., 2018). *In vivo* CT/PET imaging was performed at d0 and d7 after MPTP treatment in WT and G2019S KI mice. SPM analysis applied to test re-test assessment of CT/PET images showed a cluster of an increased normalized uptake at d7, affecting a larger portion of brain in WT with respect to G2019S KI mice (Fig. 8). SPM showed one large cluster of increased relative uptake in the olfactory bulb, cerebral cortex, striatum, hippocampus, and thalamus of WT animals (Fig. 8A, t-threshold = 3.36, t-peak = 13.2, cluster extent = 2482 voxels). Conversely, in G2019S KI mice the cluster of the relative increase was limited to the striatum (Fig. 8B, t-threshold = 3.0, t-peak *t* = 4.39, cluster extent = 391 voxels). ROI analysis on SUV revealed a trend towards an increase in both genotypes (Supplementary Tables 2–3). However, due to the high inter-subject variability, no

significant differences were observed between conditions or genotypes. Taken together, PET results indicate that MPTP produced a small increase of [^{18}F]-VC701 uptake in different brain regions of both genotypes. Moreover, SPM analysis on normalized voxels indicates that in G2019S KI mice the highest uptake was observed in striatal subregions. MPTP effects on [^{18}F]-VC701 uptake were evaluated also by *ex vivo* analysis on tissue samples, which is characterized by higher sensitivity (Fig. 9). MPTP significantly increased the radioligand uptake (SUV) in all areas examined (plasma $F_{1,30} = 21.19$, p < 0.0001; anterior cortex $F_{1,31} = 37.06$, p < 0.0001; posterior cortex $F_{1,31} = 34.86$, p < 0.0001; striatum $F_{1,31} = 53.89$, p < 0.0001; SN $F_{1,28} = 15.2$, p = 0.0006; hippocampus $F_{1,31} = 20.26$, p < 0.0001; cerebellum $F_{1,31} = 17.87$, p = 0.0002). A significant treatment X genotype interaction was found only in posterior cortex ($F_{1,31} = 4.669$, p = 0.0386) and striatum ($F_{1,31} = 6.395$, p = 0.0167) although in neither area the difference between genotypes did not reach statistical significance (p = 0.09 and p = 0.47, respectively).

To rule out differences in basal and MPTP-stimulated TSPO expression, qRT-PCR was performed. No difference in basal or MPTP-induced TSPO expression was observed between genotypes (Supplementary Fig. 6) although MPTP caused a tendency for increased TSPO expression in G2019S KI mice (p = 0.063; Supplementary Fig. 6A).

3.5. MPTP elevated GFAP expression in G2019S KI and WT mice

TSPO imaging suggested that MPTP might activate microglia and/or astrocytes in both genotypes. To confirm this view, qRT-PCR was
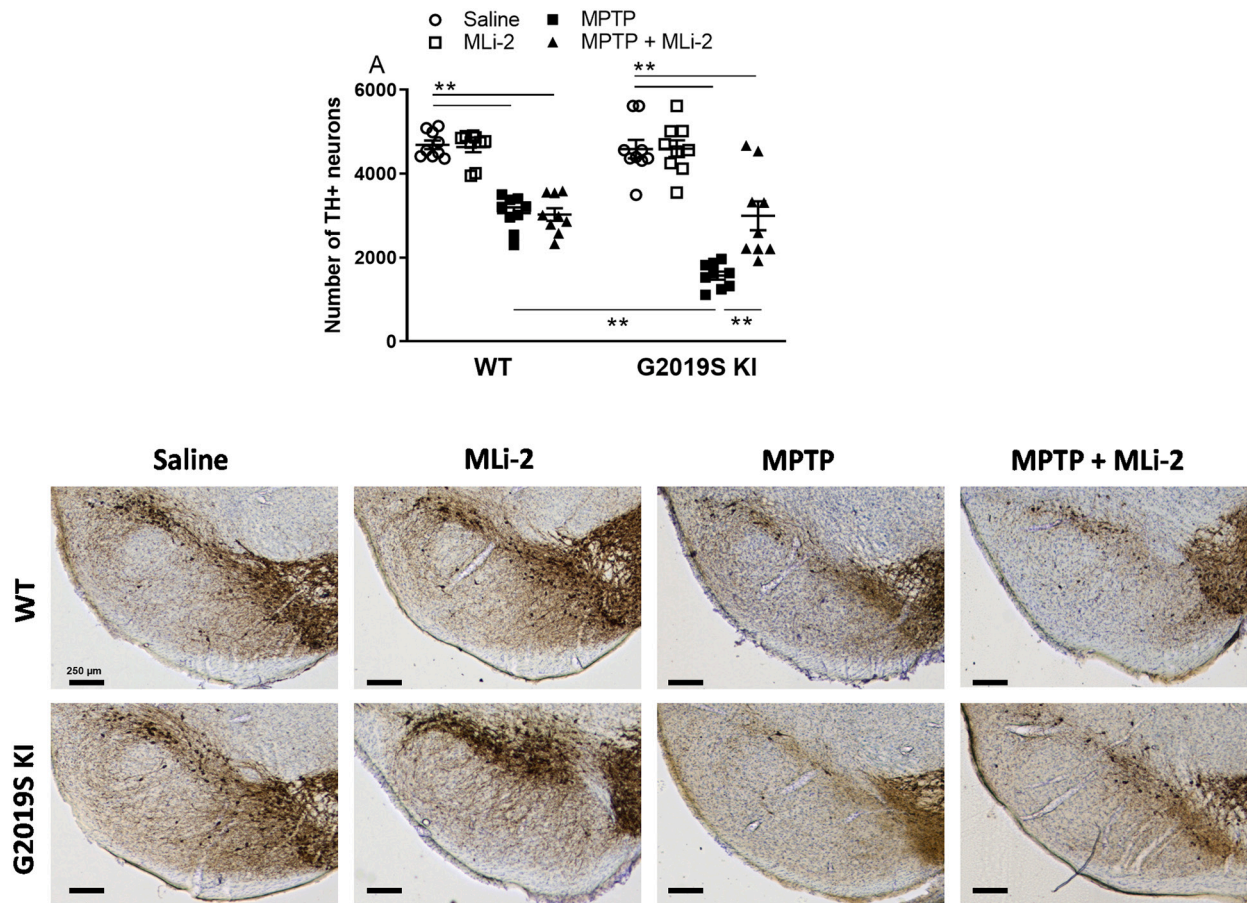
Fig. 4. Effect of therapeutic treatment with the LRRK2 inhibitor MLi-2 on MPTP-induced degeneration of dopamine (DA) neurons in the substantia nigra compacta (SNc) of G2019S KI and WT mice. Mice were administered subacute MPTP (30 mg/Kg i.p. once daily for 7 days) and starting from the 4th day onwards, also with MLi-2 (10 mg/Kg i.p. twice daily) for 10 days. Mice were euthanized 24 h after the last MLi-2 injection. Stereological quantification of tyrosine hydroxylase (TH) positive dopamine (DA) neurons in SNc, along with representative images (scale bar = 250 μm). Data represent individual values (9 mice/group), with means ± SEM. **p < 0.01 according to three-way ANOVA followed by the Tukey test for multiple comparisons.

performed. MPTP did not significantly increase the expression of TMEM-119, a specific marker of microglia (Supplementary Fig. 6B), or pro-inflammatory (iNOS, COX2; Supplementary Fig. 6C—D) or anti-inflammatory (Arg1; Supplementary Fig. 6E) genes. Conversely, a marked and quantitatively similar elevation of astrocytic marker GFAP (Supplementary Fig. 6F) was observed in WT ($t = 6.113$, df = 6, p = 0.0009) and G2019S KI ($t = 3.459$, df = 6, p = 0.0135) mice.

3.6. MLi-2 and PF-06447475 differentially modulated MPTP-induced neuroinflammation in the striatum of G2019S KI and WT mice

To shed light on the mechanisms underlying the different neuroprotective effects of LRRK2 inhibitors in striatum, the microglial response was investigated in striatal slices taken from mice exposed to MPTP and each of the two LRRK2 inhibitors in the neuroprotection study (2-week protocol). 2-way ANOVA on the number (Fig. 10A) and the area occupied (Fig. 10B) by iba-1 positive cells in the PF-06447475 study revealed a significant effect of genotype (number: $F_{1,40} = 32.36$, p < 0.0001; area $F_{1,36} = 13.36$, p = 0.0008), treatment (number $F_{2,40} = 68.75$, p < 0.0001; area $F_{2,36} = 49.86$, p < 0.0001) and a significant genotype X treatment interaction (number $F_{2,40} = 15.78$, p < 0.0001; area $F_{2,36} = 13.21$, p < 0.0001). MPTP caused larger increases of the number and the area occupied by iba-1 positive cells in G2019S KI mice with respect to WT mice. PF-06447475 did not affect the MPTP response in the striatum of WT mice but significantly reduced it in G2019S KI mice. No treatment effect on circularity, a readout for activated ameboid

microglia, was observed (Fig. 10C). A greater number by iba-1 positive cells (genotype: $F_{1,42} = 18.12$, p = 0.0001; treatment $F_{2,42} = 128.70$, p < 0.0001, time X treatment interaction $F_{2,42} = 15.27$, p < 0.0001) and their area (genotype: $F_{1,39} = 41.76$, p = 0.0001; treatment $F_{2,39} = 60.09$, p < 0.0001, time-treatment $F_{2,39} = 10.11$, p = 0.0003) in the striatum of G20919S KI mice was confirmed in the MLi-2 study (Fig. 10D-F). However, different from PF-06447475, MLi-2 increased the number (Fig. 8A) but not the total area (Fig. 10E) occupied by iba-1 positive cells in the striatum of WT mice, without affecting the microglia increase after MPTP in G2019S KI mice. Again, no effect on circularity was observed (Fig. 10F).

Finally, we evaluated whether the neuroprotective effect of MLi-2 in striatum could be due to a modulation of astrocytosis (Supplementary Fig. 7). MPTP elevated striatal GFAP staining regardless of genotype (MPTP $F_{1,16} = 93.41$ p < 0.0001; genotype X MPTP $F_{1,16} = 3.32$ p = 0.08), whereas MLi-2 alone elevated GFAP staining in WT but not G2019S KI mice (genotype X MLi-2 $F_{1,16} = 13.29$ p = 0.0022). In any genotype, however, the astrocyte response to MPTP was affected by MLi-2 (genotype X MPTP X MLi-2 $F_{1,16} = 0.219$ p = 0.65).

4. Discussion

The present study shows that G2019S LRRK2 confers greater susceptibility to nigro-striatal toxicity induced by subacute MPTP and is in line with previous studies with hG2019S BAC mice in the acute MPTP model (Arbez et al., 2020; Karuppagounder et al., 2016). Moreover, it is
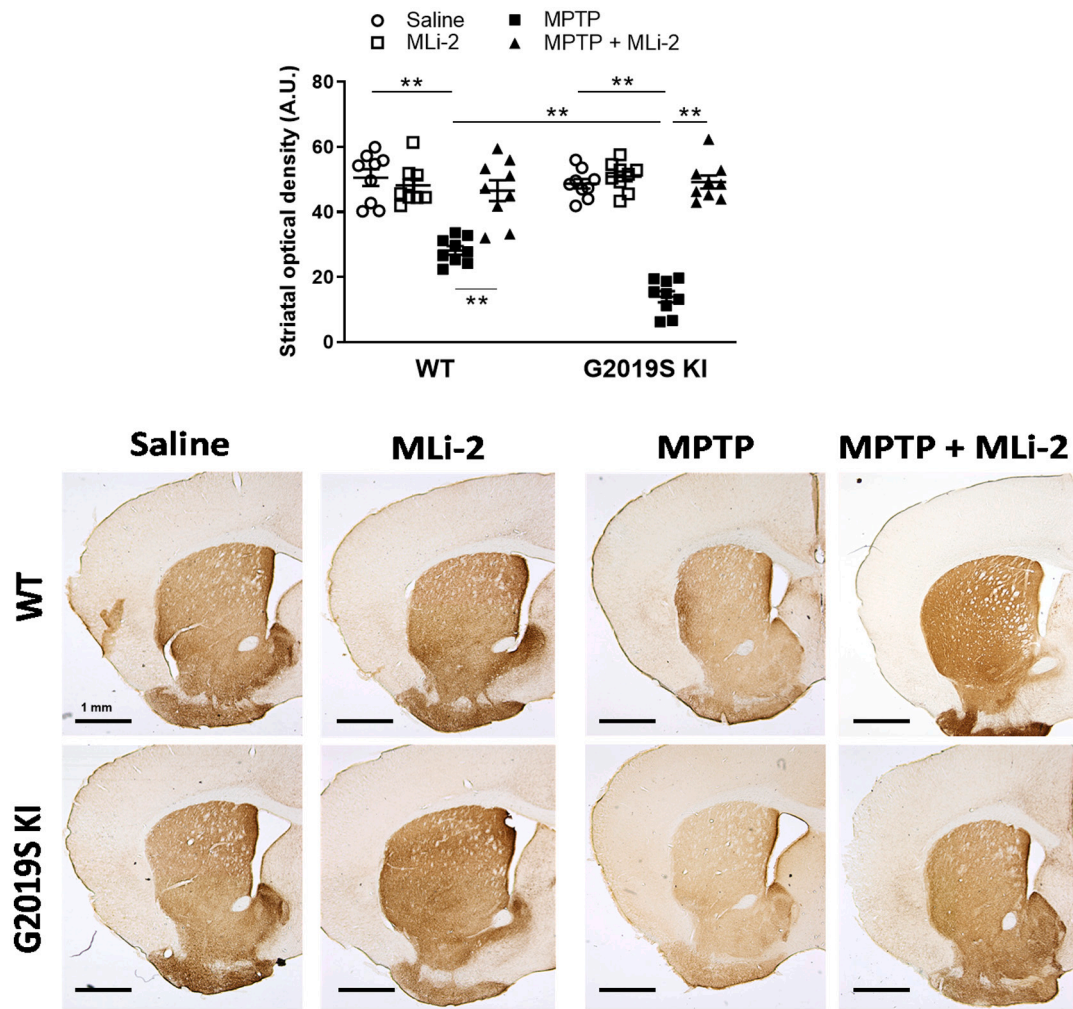
Fig. 5. Effect of therapeutic treatment with the LRRK2 inhibitor MLi-2 on MPTP-induced degeneration of tyrosine hydroxylase (TH) positive terminals in the striatum of G2019S KI and WT mice. Mice were administered subacute MPTP (30 mg/Kg i.p. once daily for 7 days) and, starting from the 4th day onwards, also with MLi-2 (10 mg/Kg i.p. twice daily) for 10 days. Mice were euthanized 24 h after the last MLi-2 injection. Optical density of TH positive terminals (greyscale arbitrary units) in the striatum, and representative images (scale bar = 1 mm). Data represent individual values (9 mice/group), with means $\pm$ SEM. **$p < 0.01$ according to three-way ANOVA followed by the Tukey test for multiple comparisons.
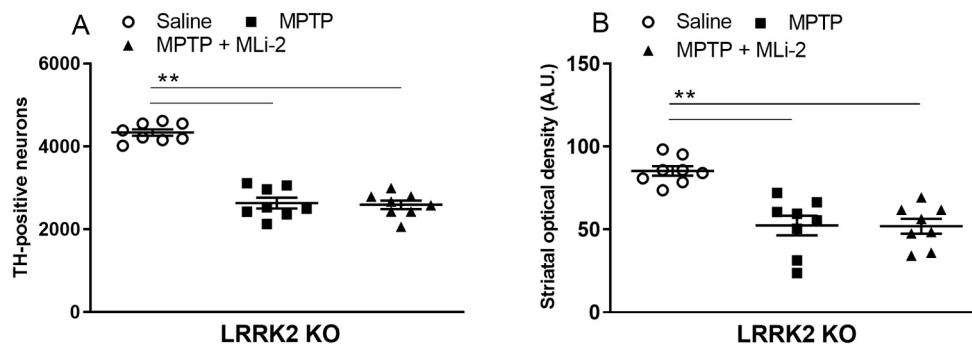

Fig. 6. The LRRK2 inhibitor MLi-2 does not rescue LRRK2 KO mice from MPTP-induced nigro-striatal dopamine (DA) neuron degeneration. Mice were administered subacute MPTP (30 mg/Kg i.p. once daily for 7 days) and, starting from the 4th day onwards, also with MLi-2 (10 mg/Kg i.p. twice daily) for 10 days. Mice were euthanized 24 h after the last MLi-2 injection. Stereological quantification of tyrosine hydroxylase (TH) positive DA neurons in substantia nigra compacta (SNc) (A) and optical density of TH positive terminals in striatum (B). Data are expressed as number of TH positive neurons and striatal optical density (grey scale arbitrary units) and represent 8 mice per group with mean $\pm$ SEM. **$p < 0.01$ according to one-way ANOVA followed by the Tukey test for multiple comparisons.

consistent with the larger reduction of field potential amplitude, an index of deranged neurotransmission, in striatal slices of G2019S KI mice exposed to rotenone (Tozzi et al., 2018). Two lines of evidence suggest that the enhanced LRRK2 kinase activity is instrumental to the greater LRRK2 G2019S toxicity in this MPTP model of parkinsonism. In fact, neither LRRK2 KO nor KD mice showed enhanced sensitivity to MPTP, and small molecule LRRK2 kinase inhibitors PF-06447475 and MLi-2 were able to reverse it. Previous studies proved that PF-06447475
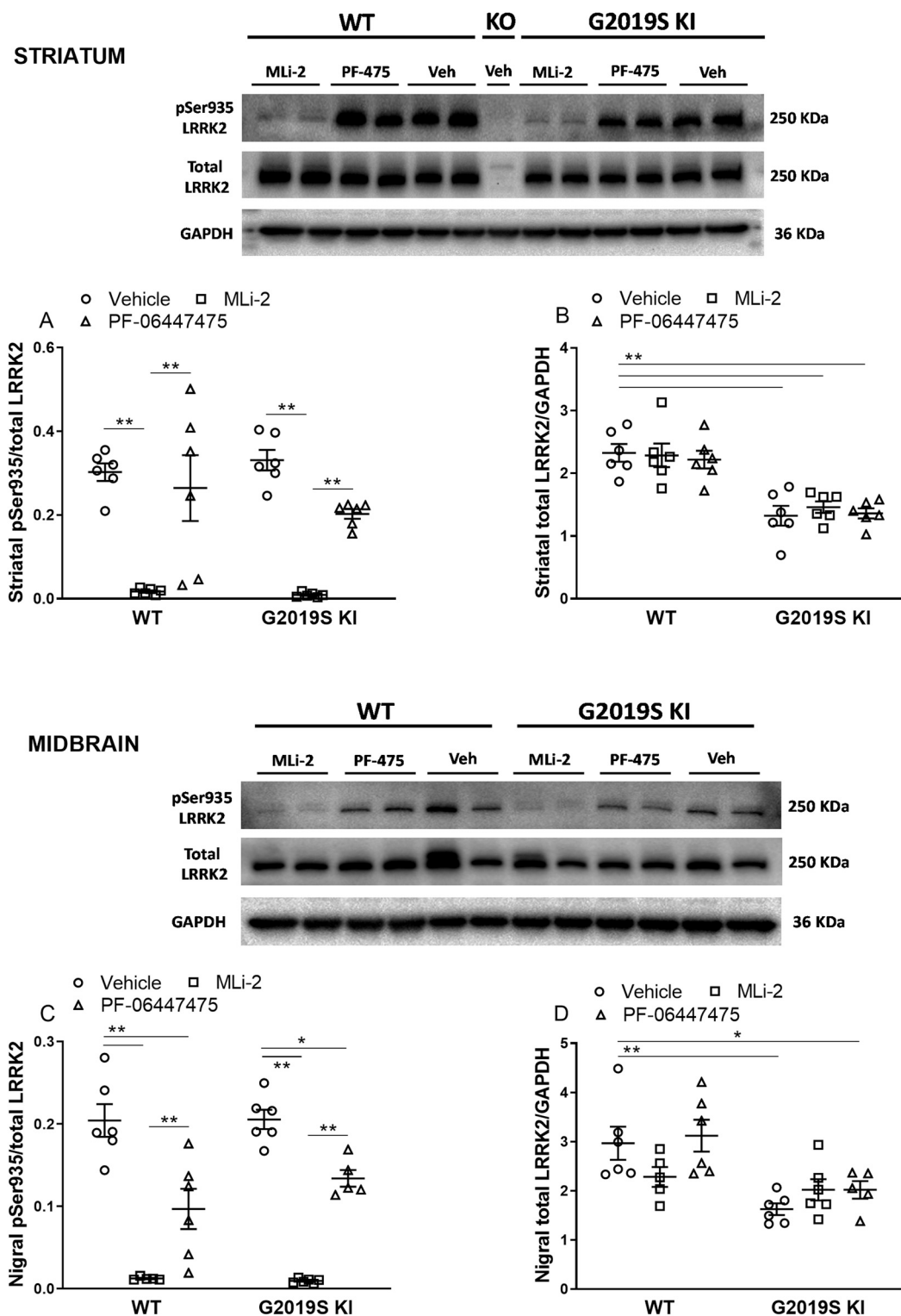
Fig. 7. Target validation in WT and G2019S KI mice. Mice were treated with the LRRK2 inhibitors PF-06447475 and MLi-2 (10 mg/Kg, twice daily, i.p.) or vehicle for 10 days and euthanized 2 h after the last injection. The striatum and midbrain were excised and processed for Western blot analysis. The phosphorylation levels of Serine 935 LRRK2, a readout of kinase activity, were measured and expressed as ratio to total LRRK2 (A, C). LRRK2 levels (B, D) were compared against the housekeeping GAPDH. In midbrain homogenates, TH levels were also quantified to confirm correct tissue sampling (see Supplementary materials). Data represent individual values (6 mice/group), with mean ± SEM. *p < 0.05, **p < 0.01 according to two-way ANOVA followed by the Tukey test for multiple comparisons.

or its analog PFE-360 are neuroprotective against α-syn-induced parkinsonism in hG2019S overexpressing rats (Daher et al., 2015) or in rats where hG2019S LRRK2 was virally overexpressed (although in this study a destabilizing effect of PFE-360 on the human protein was found)

(Nguyen et al., 2020). Nonetheless, the same evidence was lacking for MLi-2 and this study fills this scientific gap. Actually, MLi-2 rescued striatal TH positive nerve terminals not only in G2019S KI mice but also in WT mice. This effect truly relied on LRRK2 since no protection was
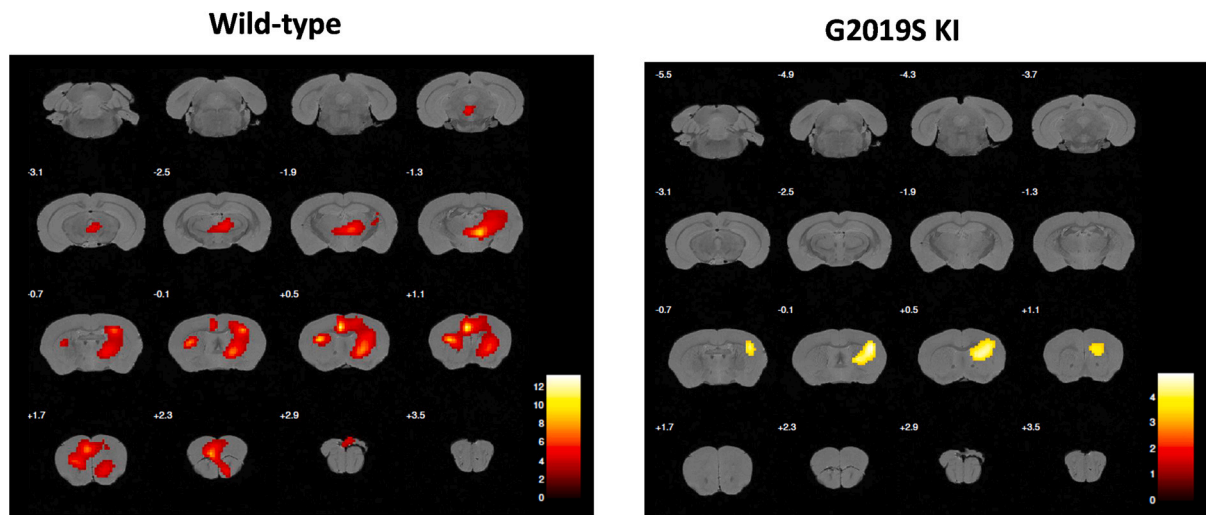
Wild-type　　　　　　　　　　　　　　**G2019S KI**

Fig. 8. *In vivo* CT/PET imaging test-retest with [^{18}F]-VC701 in MPTP-treated G2019S KI and WT mice. Longitudinal brain evaluation of [^{18}F]-VC701 uptake in WT and G2019S KI animals treated with MPTP (30 mg/Kg i.p. once daily for 7 days) and tested before (d0) and after the last injection (d7): test-retest study. SPM results in WT (A) and G2019S KI (B) mice. The color scale of blobs superimposed on the brain atlas represents the t-value of the *t*-test in each voxel. The cluster defining threshold was set at p < 0.01.

observed in MPTP-treated LRRK2 KO mice, suggesting that MLi-2 might be effective against not only familial G2019S LRRK2-associated PD but also iPD. The interest for the role of LRRK2 in iPD has been fueled by the finding that LRRK2 is activated in the brain of iPD patients (Di Maio et al., 2018). However, some studies reported that genetic or pharmacological (*via* antisense nucleotides) deletion of LRRK2 protected from genetic (Lin et al., 2009) or viral (Daher et al., 2014) hα-syn overexpression, PFF injection (Zhao et al., 2017), LPS/paraquat (Dwyer et al., 2020) or rotenone (Rocha et al., 2020) administration whereas other studies failed to prove so (Andres-Mateos et al., 2009; Van der Perren et al., 2021). Consistent with LRRK2 not contributing to iPD, MLi-2 or PF-360 failed to alter PD-like neurochemical and functional changes in MitoPark mice (Fell et al., 2015) or protected from nigrostriatal degeneration rodents injected with α-syn PFFs (Henderson et al., 2019) or AAV hα-syn (Kelly et al., 2021; Van der Perren et al., 2021). Only one study reported neuroprotection with subacute PFE-360 (10 mg/Kg twice daily p.o.) in WT rats treated with rotenone (Rocha et al., 2020), which supports MLi-2 efficacy in MPTP-treated WT mice observed herein. Perhaps, two main factors influenced the outcome of these neuroprotection studies: the model employed, which can be associated with a different degree of endogenous LRRK2 activation, and the degree of LRRK2 inhibition achieved with the LRRK2 inhibitor. Indeed, although both PF-06447475 and MLi-2 rescued nigral DA neurons from MPTP-induced neurodegeneration, only MLi-2 was neuroprotective in striatum, but this different response correlated with the different degree of LRRK2 inhibition achieved in this area. Indeed, MLi-2 abolished striatal pSer935 LRRK2 levels in both WT and G2019S KI mice whereas PF-06447475 was ineffective in WT mice and showed only a trend to inhibition in G2019S KI mice. MLi-2 is ~4-fold more potent than PF-06447475 in inhibiting purified LRRK2 (IC$_{50}$ 0.76 nM and 3 nM, respectively) and ~ 18-fold more potent than PF-06447475 in Ser935 dephosphorylation (IC$_{50}$ 1.4 nM and 24 nM, respectively) *in vitro* (Fell et al., 2015; Henderson et al., 2015). Since MLi-2 and PF-360 (a close analog of PF-06447475) have similar pharmacokinetic properties (Kelly et al., 2018), using the same dose for both inhibitors might have generated striatal drug concentrations with maximal (MLi-2) or negligible (PF-06447475) LRRK2 inhibitory efficacy. Both compounds are highly brain penetrant and were used at doses derived from seminal studies of (Fell et al., 2015) (MLi-2) and (Henderson et al., 2015) (PF-06447475), followed by others (Kelly et al., 2021; Kelly et al., 2018; Kluss et al., 2018; Kluss et al., 2021; Van der Perren et al., 2021). For

MLi-2 we adopted a b.i.d. administration protocol of 10 mg/Kg i.p. considering the almost complete abrogation of pSer935 levels after single administration of 3 mg/Kg s.c. (Kluss et al., 2018) or 10 mg/Kg p. o. (Fell et al., 2015; Kluss et al., 2021), and the short half-life of the compound (Fell et al., 2015; Kelly et al., 2018). A similar protocol (10 mg/Kg p.o. b.i.d. for 5 days) was also adopted in rats by (Van der Perren et al., 2021). For PF-06447475, we administered 10 mg/Kg i.p. b.i.d. due to the ~90% inhibition of pSer935 levels observed in WT mice administered s.c. with the same dose, and the relative short half-life of the compound (Henderson et al., 2015). PF-06447475 (3–30 mg/Kg p.o. b.i.d.) was used by another group in rats (Daher et al., 2015; Kelly et al., 2021). Our data confirm that LRRK2 dephosphorylated in response to LRRK2 inhibitors and that pSer935 levels are reliable marker of LRRK2 kinase activity in both WT and G2019S KI mice. Different from pSer935 levels, pRab10 levels did not correlate with LRRK2 kinase inhibition in striatal homogenates. This agrees with previous studies in mice (Kelly et al., 2018; Kluss et al., 2021) where pRab12, instead, proved to be a reliable marker of LRRK2 kinase activity (Kluss et al., 2021). The lack of response might be due to the animal species and strain, given that Rab10 levels show strain dependence (Kelly et al., 2021). Moreover, since Rab10 expression, different from LRRK2 expression, is heterogeneous across the different cell populations, tissue homogenates might not a suitable preparation to measure target validation using pRab10 as a readout (Kelly et al., 2018).

It is noteworthy that, in keeping with previous *in vivo* studies with PF-06447475 (Daher et al., 2015; Kelly et al., 2021), PFE-360 (Andersen et al., 2018; Kelly et al., 2021) or MLi-2 (Fell et al., 2015; Henderson et al., 2019; Kluss et al., 2021), abrogation of pSer935 levels did not affect brain LRRK2 levels and was well tolerated. Intriguingly, the midbrain pattern was different from striatum, since PF-06447475 partially inhibited pSer935 levels in WT and G2019S KI mice, and was equally effective as MLi-2 in preventing MPTP-induced neurodegeneration. It is possible that due to the lower levels of endogenous LRRK2 in this region compared to the striatum, neuroprotection in SNc can be achieved also at a lower level of LRRK2 kinase inhibition and, therefore, also with the less potent inhibitor. However, despite MLi-2 abrogated pSer935 LRRK2 levels also in midbrain, it was only able to rescue the hypersensitivity of nigral G2019S neurons to MPTP, being unable to protect nigral DA cells from the toxin in any genotype. Therefore, in the MPTP model, additional mechanisms might be active at the nigral level that are insensitive to LRRK2 kinase inhibition. The
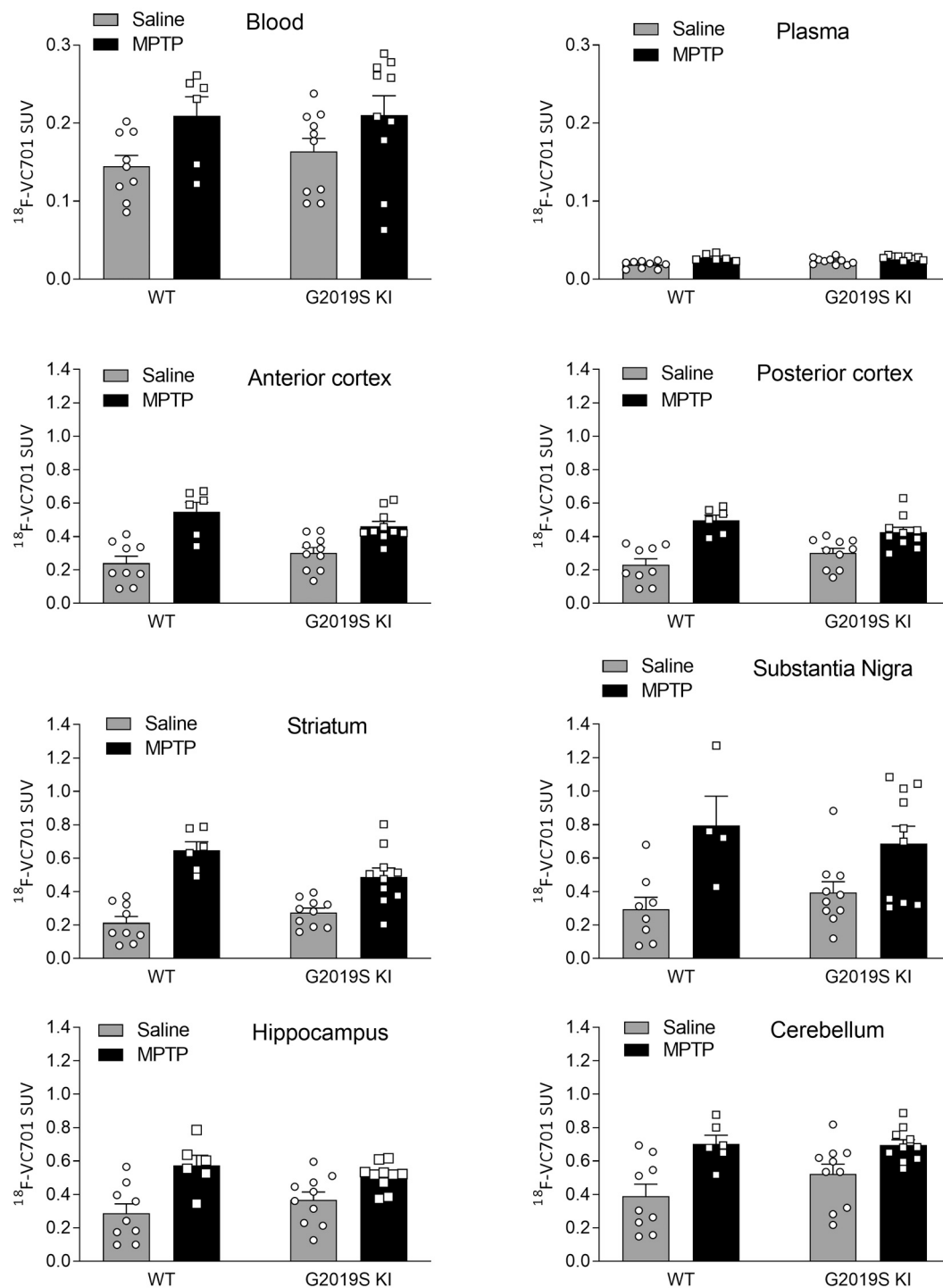
Fig. 9. *Ex-vivo* [^{18}F]-VC701 brain tissue sampling in G2019S KI and WT mice. Mice were treated with MPTP (30 mg/Kg i.p. once daily) or saline for 7 days, then euthanized 4 h after the last MPTP injection and 2 h after radiotracer injection. Radioactivity values in blood and plasma samples (A-B) and regional tracer distribution in anterior (C) and posterior (D) cortex, striatum (E), substantia nigra (F), hippocampus (G), and cerebellum (H) in G2019S KI and WT mice 7 days after administration. Data are expressed as mean ± SEM Standardized Uptake Value (SUV) and show individual values (n = 9 WT vehicle, n = 10 G2019S KI vehicle, n = 6 WT MPTP, n = 10 G2019S KI MPTP) with means ± SEM.

paradoxical finding that MLi-2 prevented striatal DA terminal loss in MPTP-treated WT mice while LRRK2 KO mice were not protected from MPTP might be explained considering that the *LRRK2* homolog, *LRRK1*, might compensate for the loss of LRRK2, since their tissue expression, particularly during development, is coordinated (Biskup et al., 2007). In adult mice, however, only LRRK2 is expressed in nigro-striatal neurons, thus acute blockade of LRRK2 might leave uncompensated cellular

functions regulated by LRRK1. Indeed, constitutive genetic deletion of both *LRRK2* and *LRRK1*, but not either gene alone, resulted in the early onset of a parkinsonian phenotype and loss of nigral DA neurons (Giaime et al., 2017).

With respect to the factors determining the higher sensitivity of G2019S KI mice to mitochondrial complex I inhibition, several studies have reported mitochondrial morphological aberrations or dysfunctions
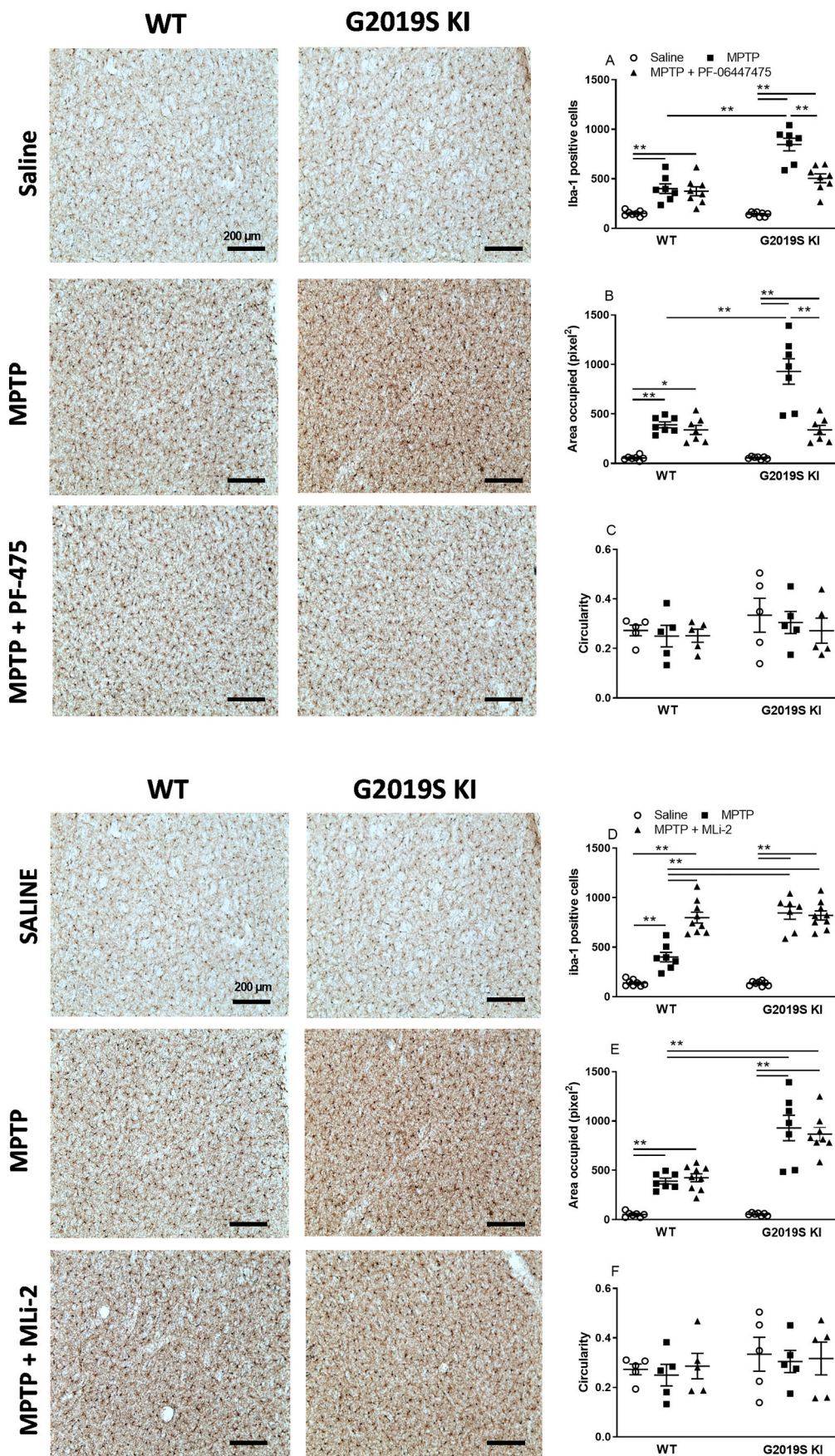
Fig. 10. Effect of therapeutic treatments with the LRRK2 inhibitors PF-06447475 and MLi-2 on iba-1 immunoreactivity in the striatum of G2019S KI and WT mice. Mice were administered subacute MPTP (30 mg/Kg once daily i.p. for 7 days) and starting from the 4th day onwards, also with PF-06447475 or MLi-2 (10 mg/Kg twice daily i.p., each) for 10 days. Mice were euthanized 24 h after the last LRRK2 inhibitor injection. Quantification of iba-1-positive cells (A,D), their area (B,E) and circularity (C,F), along with representative images (scale bar = 200 μm). Data are expressed as individual mice (n = 7–8/group in panels A,B,D,E, and n = 5/group in panels C,F) with means ± SEM. **p<0.01 according to two-way ANOVA followed by the Tukey test for multiple comparisons.

in G2019S KI mice (Yue et al., 2015), or astrocytes (Ramos-Gonzalez et al., 2021), fibroblasts (Mortiboys et al., 2010) and iPSC (Cooper et al., 2012; Sanders et al., 2014) from LRRK2 G2019S patients, and even SH-SY-5Y cells overexpressing G2019S LRRK2 (Tozzi et al., 2018). In these cells, specifically, the sensitivity to rotenone manifested as a greater elevation of ROS production and reductions of Ca^{2+} levels and ATP synthesis compared to WT cells, accompanied by abnormal morphology (Tozzi et al., 2018), suggesting a critical effect of LRRK2 on mitochondrial function. Both cell autonomous and non-cell autonomous mechanisms might underlie the higher sensitivity of nigral DA neurons to MPTP. In fact, the elevation of iba-1 and GFAP immunoreactivity in striatum confirmed that subacute MPTP causes microgliosis and astrogliosis (Lee et al., 2019; Qiao et al., 2020). The finding that microglia recruitment was greater in G2019S KI mice is consistent with the well-described pro-inflammatory role of G2019S LRRK2 (Ma et al., 2016; Moehle et al., 2012; Russo et al., 2015). However, whether blockade of the MPTP-induced inflammatory response underlies the neuroprotective effects of LRRK2 inhibitors and, particularly, MLi-2 in striatum is a matter of speculation. In fact, PF-06447475 failed to rescue striatal TH terminals and did not attenuate the increased striatal microglial response in MPTP-treated WT mice, albeit reducing it in G2019S KI mice. This is consistent with that found in the SNc of hG2019S transgenic *vs* non transgenic rats (Daher et al., 2015) although PF-06447475 attenuated the loss of both nigral DA cells and striatal DA terminals in G2019S transgenic rats (Daher et al., 2015). G2019S overexpression in hG2019S transgenic rats and/or the higher degree of LRRK2 inhibition achieved in that study (Daher et al., 2015) might explain the discrepancy. Surprisingly, however, MLi-2 further amplified the increase of iba-1 positive cells induced by MPTP in WT mice but did not change the MPTP response in G2019S KI mice, providing striatal protection in both genotypes. Further analysis also at earlier time points is needed to establish whether MLi-2 causes striatal neuroprotection through modulation of the microglial response. In fact, microglia are transiently activated during the first days of repeated MPTP treatment (Drouin-Ouellet et al., 2011) and, consistently, analysis of circularity suggests that iba-1 positive cells are less activated a week after MPTP withdrawal. The finding that the expression of TMEM119, a specific homeostatic microglia marker (Satoh et al., 2016), remained unchanged after MPTP withdrawal might support this view. Therefore, the possibility that the higher number of iba-1 positive cells in MPTP-treated mice is due to infiltrating macrophages should be considered. In fact, iba-1 does not discriminate among microglia and infiltrating macrophages (Davoust et al., 2008), and prolonged MPTP administration is associated with a long-lasting increase (up to 14 days after MPTP withdrawal) infiltration of bone-marrow-derived cells in dopaminergic damaged areas (Rodriguez et al., 2007). Whether these cells play a detrimental or beneficial role remains to be determined. However, the finding that MLi-2 enhanced the number of MPTP-induced iba-1 positive cells in WT mice might suggest that LRRK2 inhibition promotes the recruitment of macrophages/microglia with neuroprotective functions (Barnum and Tansey, 2010; Teismann et al., 2003). The finding that MLi-2 did not attenuate the MPTP-induced astrocyte activation in the striatum of WT and G2019S KI mice argues against the possibility that striatal neuroprotection was achieved through attenuation of MPTP-induced astrogliosis. Indeed, astrocytes can have both beneficial and detrimental effect on neuronal function (Booth et al., 2017). We should, however, note that MLi-2 was able to elevate GFAP immunoreactivity in WT mice, thus occluding the effect of MPTP. The view that LRRK2 kinase inhibition might cause astrocyte deregulation, thereby favoring protection against MPTP, is in line with LRRK2 kinase being a negative regulator of astrocyte function. In fact, genetic deletion or pharmacological inhibition of LRRK2 improved lysosomal function in WT astrocytes (Henry et al., 2015; Sanyal et al., 2020). Why MLi-2 would increase GFAP signaling specifically in WT mice is unclear, although G2019S LRRK2 is associated with dramatic changes of astrocyte homeostasis (Streubel-Gallasch et al., 2021) (Ramos-Gonzalez et al., 2021) which might be

kinase-independent or not reversable under short-term kinase inhibition.

An increase of the binding of the TSPO PET tracer [11C]-PK11195 was previously observed in mice acutely treated with MPTP (Belloli et al., 2020; Belloli et al., 2018). Such an increase is presently replicated in the subacute MPTP model using the novel TSPO tracer [18F]-VC701. In the absence of a reference region for SPM analysis to reduce inter-subject variability, voxels were normalized to mean global values of every single subject, showing a treatment effect in both genotypes with a large anatomical involvement in WT mice and a limited effect (striatum) in G2019S KI mice. ROI analysis indicated a modest but consistent increase in tracer uptake in different brain regions including striatum, cortex, hippocampus, and thalamus, as previously observed in the acute MPTP model (Belloli et al., 2018). However, due to the low sensitivity and spatial resolution of PET together with the small increase of binding observed, the effect was scattered, particularly in G2019S KI mice, and did not reach a significant threshold. This drawback was overcome by *ex vivo* sampling, which revealed a significant increase of similar magnitude in different brain regions of both genotypes, again with greater variability in G2019S KI mice. Considering that TSPO is upregulated in microglia/macrophages and astrocytes during the proinflammatory status (Beckers et al., 2018; Pannell et al., 2020), for the reasons detailed above, the greater uptake of [18F]-VC701 seems more consistent with astrocyte rather than microglia activation, which is independent of genotype, as also confirmed by striatal GFAP immunoreactivity.

In conclusion, the present study offers novel *in vivo* evidence that G2019S KI mice are more susceptible to the nigro-striatal degeneration induced by Complex I inhibitor MPTP, and that this susceptibility relies on the increased LRRK2 kinase activity. Besides, it reports for the first time the neuroprotective effect of MLi-2 in a model of parkinsonism. This study also provides the first evidence of TSPO PET imaging in living G2019S KI mice, although further tests are needed to validate this tool as a marker of neuroinflammation (Belloli et al., 2020). Altogether, these data confirm that G2019S LRRK2 confers greater susceptibility to environmental parkinsonian toxins (Rocha et al., 2020), and G2019S KI mice might represent a model of presymptomatic/premotor PD useful to investigate the etiology of PD through the interplay of genetic, intrinsic, and environmental factors (Longo et al., 2017; Novello et al., 2018).

Availability of supporting data

The datasets generated during and/or analyzed during the current study are available from the corresponding author on reasonable request.

Funding

Author's contribution

SN injected MPTP and perfused the animals, performed TH and iba-1 immunohistochemistry and stereological counting, analyzed the data and drafted the manuscript; DM injected MPTP and perfused the animals, performed immunohistochemistry; FA injected MPTP, perfused the animals, performed immunohistochemistry and stereological counting; CD and AB injected LRRK2 inhibitors and assessed animal behavior; CD performed Western analysis and GFAP immunostaining. SV performed immunohistochemistry; SD performed stereological counting, ED and MB performed qRT-PCR and analyzed the data, VM, LP, SB injected MPTP, performed imaging and analyzed the data, DRS,

EB and RMM drafted the manuscript and coordinated the study, MM conceived and coordinated the study, analyzed the data, drafted and prepared the manuscript. All authors read, revised, and approved the final manuscript.

Declaration of Competing Interest

DRS is an employee of Novartis Pharma AG. The other authors report no competing financial interests.

Acknowledgements

Appendix A. Supplementary data

Supplementary data to this article can be found online at https://doi.org/10.1016/j.nbd.2021.105579.

References

Albanese, F., et al., 2021. Constitutive silencing of LRRK2 kinase activity leads to early glucocerebrosidase deregulation and late impairment of autophagy in vivo. Neurobiol. Dis. 159, 105487.

Andersen, M.A., et al., 2018. Parkinson's disease-like burst firing activity in subthalamic nucleus induced by AAV-alpha-synuclein is normalized by LRRK2 modulation. Neurobiol. Dis. 116, 13–27.

Andres-Mateos, E., et al., 2009. Unexpected lack of hypersensitivity in LRRK2 knock-out mice to MPTP (1-methyl-4-phenyl-1,2,3,6-tetrahydropyridine). J. Neurosci. 29, 15846–15850.

Arbez, N., et al., 2020. G2019S-LRRK2 mutation enhances MPTP-linked parkinsonism in mice. Hum. Mol. Genet. 29, 580–590.

Ashburner, J., Friston, K.J., 1999. Nonlinear spatial normalization using basis functions. Hum. Brain Mapp. 7, 254–266.

Barnum, C.J., Tansey, M.G., 2010. Modeling neuroinflammatory pathogenesis of Parkinson's disease. Prog. Brain Res. 184, 113–132.

Beccano-Kelly, D.A., et al., 2014. Synaptic function is modulated by LRRK2 and glutamate release is increased in cortical neurons of G2019S LRRK2 knock-in mice. Front. Cell. Neurosci. 8, 301.

Beckers, L., et al., 2018. Neuronal dysfunction and behavioral abnormalities are evoked by neural cells and aggravated by inflammatory microglia in peroxisomal beta-oxidation deficiency. Front. Cell. Neurosci. 12, 136.

Belloli, S., et al., 2018. (18)F-VC701-PET and MRI in the in vivo neuroinflammation assessment of a mouse model of multiple sclerosis. J. Neuroinflammation 15, 33.

Belloli, S., et al., 2020. Translation imaging in Parkinson's disease: focus on neuroinflammation. Front. Aging Neurosci. 12, 152.

Betarbet, R., et al., 2002. Animal models of Parkinson's disease. Bioessays 24, 308–318.

Biskup, S., et al., 2007. Dynamic and redundant regulation of LRRK2 and LRRK1 expression. BMC Neurosci. 8, 102.

Booth, H.D.E., et al., 2017. The role of astrocyte dysfunction in Parkinson's disease pathogenesis. Trends Neurosci. 40, 358–370.

Cooper, O., et al., 2012. Pharmacological rescue of mitochondrial deficits in iPSC-derived neural cells from patients with familial Parkinson's disease. Sci. Transl. Med. 4, 141ra90.

Correia Guedes, L., et al., 2010. Worldwide frequency of G2019S LRRK2 mutation in Parkinson's disease: a systematic review. Parkinsonism Relat. Disord. 16, 237–242.

Daher, J.P., et al., 2014. Abrogation of alpha-synuclein-mediated dopaminergic neurodegeneration in LRRK2-deficient rats. Proc. Natl. Acad. Sci. U. S. A. 111, 9289–9294.

Daher, J.P., et al., 2015. Leucine-rich repeat kinase 2 (LRRK2) pharmacological inhibition abates alpha-Synuclein gene-induced neurodegeneration. J. Biol. Chem. 290, 19433–19444.

Davoust, N., et al., 2008. From bone marrow to microglia: barriers and avenues. Trends Immunol. 29, 227–234.

Deng, X., et al., 2011. Characterization of a selective inhibitor of the Parkinson's disease kinase LRRK2. Nat. Chem. Biol. 7, 203–205.

Di Grigoli, G., et al., 2015. Radiosynthesis and preliminary biological evaluation of [18F]VC701, a Radioligand for translocator protein. Mol. Imaging 14.

Di Maio, R., et al., 2018. LRRK2 activation in idiopathic Parkinson's disease. Sci. Transl. Med. 10.

Drouin-Ouellet, J., et al., 2011. The role of the MYD88-dependent pathway in MPTP-induced brain dopaminergic degeneration. J. Neuroinflammation 8, 137.

Dwyer, Z., et al., 2020. Leucine-rich repeat kinase-2 (LRRK2) modulates microglial phenotype and dopaminergic neurodegeneration. Neurobiol. Aging 91, 45–55.

Dzamko, N., et al., 2010. Inhibition of LRRK2 kinase activity leads to dephosphorylation of Ser(910)/Ser(935), disruption of 14-3-3 binding and altered cytoplasmic localization. Biochem. J. 430, 405–413.

Fell, M.J., et al., 2015. MLi-2, a potent, selective, and centrally active compound for exploring the therapeutic potential and safety of LRRK2 kinase inhibition. J. Pharmacol. Exp. Ther. 355, 397–409.

Fuji, R.N., et al., 2015. Effect of selective LRRK2 kinase inhibition on nonhuman primate lung. Sci. Transl. Med. 7, 273ra15.

Giaime, E., et al., 2017. Age-dependent dopaminergic neurodegeneration and impairment of the autophagy-lysosomal pathway in LRRK-deficient mice. Neuron 96 (796–807), e6.

Greggio, E., et al., 2006. Kinase activity is required for the toxic effects of mutant LRRK2/dardarin. Neurobiol. Dis. 23, 329–341.

Healy, D.G., et al., 2008. Phenotype, genotype, and worldwide genetic penetrance of LRRK2-associated Parkinson's disease: a case-control study. Lancet Neurol. 7, 583–590.

Henderson, J.L., et al., 2015. Discovery and preclinical profiling of 3-[4-(morpholin-4-yl)-7H-pyrrolo[2,3-d]pyrimidin-5-yl]benzonitrile (PF-06447475), a highly potent, selective, brain penetrant, and in vivo active LRRK2 kinase inhibitor. J. Med. Chem. 58, 419–432.

Henderson, M.X., et al., 2018. LRRK2 activity does not dramatically alter alpha-synuclein pathology in primary neurons. Acta Neuropathol. Commun. 6, 45.

Henderson, M.X., et al., 2019. LRRK2 inhibition does not impart protection from alpha-synuclein pathology and neuron death in non-transgenic mice. Acta Neuropathol. Commun. 7, 28.

Henry, A.G., et al., 2015. Pathogenic LRRK2 mutations, through increased kinase activity, produce enlarged lysosomes with reduced degradative capacity and increase ATP13A2 expression. Hum. Mol. Genet. 24, 6013–6028.

Herzig, M.C., et al., 2011. LRRK2 protein levels are determined by kinase function and are crucial for kidney and lung homeostasis in mice. Hum. Mol. Genet. 20, 4209–4223.

Hinkle, K.M., et al., 2012. LRRK2 knockout mice have an intact dopaminergic system but display alterations in exploratory and motor co-ordination behaviors. Mol. Neurodegener. 7, 25.

Ito, G., et al., 2016. Phos-tag analysis of Rab10 phosphorylation by LRRK2: a powerful assay for assessing kinase function and inhibitors. Biochem. J. 473, 2671–2685.

Kalia, L.V., et al., 2015. Clinical correlations with Lewy body pathology in LRRK2-related Parkinson disease. JAMA Neurol. 72, 100–105.

Karuppagounder, S.S., et al., 2016. LRRK2 G2019S transgenic mice display increased susceptibility to 1-methyl-4-phenyl-1,2,3,6-tetrahydropyridine (MPTP)-mediated neurotoxicity. J. Chem. Neuroanat. 76, 90–97.

Kelly, K., et al., 2018. The G2019S mutation in LRRK2 imparts resiliency to kinase inhibition. Exp. Neurol. 309, 1–13.

Kelly, K., et al., 2021. Genetic background influences LRRK2-mediated Rab phosphorylation in the rat brain. Brain Res. 1759, 147372.

Kluss, J.H., et al., 2018. Detection of endogenous S1292 LRRK2 autophosphorylation in mouse tissue as a readout for kinase activity. NPJ Parkinsons Dis. 4, 13.

Kluss, J.H., et al., 2021. Preclinical modeling of chronic inhibition of the Parkinson's disease associated kinase LRRK2 reveals altered function of the endolysosomal system in vivo. Mol. Neurodegener. 16, 17.

Lee, B.D., et al., 2010. Inhibitors of leucine-rich repeat kinase-2 protect against models of Parkinson's disease. Nat. Med. 16, 998–1000.

Lee, E., et al., 2019. MPTP-driven NLRP3 inflammasome activation in microglia plays a central role in dopaminergic neurodegeneration. Cell Death Differ. 26, 213–228.

Lin, X., et al., 2009. Leucine-rich repeat kinase 2 regulates the progression of neuropathology induced by Parkinson's-disease-related mutant alpha-synuclein. Neuron. 64, 807–827.

Longo, F., et al., 2014. Genetic and pharmacological evidence that G2019S LRRK2 confers a hyperkinetic phenotype, resistant to motor decline associated with aging. Neurobiol. Dis. 71, 62–73.

Longo, F., et al., 2017. Age-dependent dopamine transporter dysfunction and Serine129 phospho-alpha-synuclein overload in G2019S LRRK2 mice. Acta Neuropathol. Commun. 5, 22.

Ma, Y., et al., 2005. A three-dimensional digital atlas database of the adult C57BL/6J mouse brain by magnetic resonance microscopy. Neuroscience. 135, 1203–1215.

Ma, B., et al., 2016. LRRK2 modulates microglial activity through regulation of chemokine (C-X3-C) receptor 1 -mediated signalling pathways. Hum. Mol. Genet. 25, 3515–3523.

Mercatelli, D., et al., 2019. Leucine-rich repeat kinase 2 (LRRK2) inhibitors differentially modulate glutamate release and Serine935 LRRK2 phosphorylation in striatal and cerebrocortical synaptosomes. Pharmacol. Res. Perspect. 7, e00484.

Mestre, T.A., et al., 2018. Clustering of motor and nonmotor traits in leucine-rich repeat kinase 2 G2019S Parkinson's disease nonparkinsonian relatives: a multicenter family study. Mov. Disord. 33, 960–965.

Migheli, R., et al., 2013. LRRK2 affects vesicle trafficking, neurotransmitter extracellular level and membrane receptor localization. PLoS One 8, e77198.

Moehle, M.S., et al., 2012. LRRK2 inhibition attenuates microglial inflammatory responses. J. Neurosci. 32, 1602–1611.

Mortiboys, H., et al., 2010. Mitochondrial impairment in patients with Parkinson disease with the G2019S mutation in LRRK2. Neurology. 75, 2017–2020.

Nguyen, A.P.T., et al., 2020. Dopaminergic neurodegeneration induced by Parkinson's disease-linked G2019S LRRK2 is dependent on kinase and GTPase activity. Proc. Natl. Acad. Sci. U. S. A. 117, 17296–17307.

Novello, S., et al., 2018. G2019S LRRK2 mutation facilitates alpha-synuclein neuropathology in aged mice. Neurobiol. Dis. 120, 21–33.

Oueslati, A., 2016. Implication of alpha-Synuclein phosphorylation at S129 in Synucleinopathies: what have we learned in the last decade? J. Parkinsons Dis. 6, 39–51.

Pannell, M., et al., 2020. Imaging of translocator protein upregulation is selective for pro-inflammatory polarized astrocytes and microglia. Glia. 68, 280–297.

Paxinos, G., Franklin, K.B.J., 2001. The Mouse Brain in Stereotaxic Coordinates. Academic Press, San Diego.

Qiao, C.M., et al., 2020. Sodium butyrate exacerbates Parkinson's disease by aggravating Neuroinflammation and colonic inflammation in MPTP-induced mice model. Neurochem. Res. 45, 2128–2142.

Ramos-Gonzalez, P., et al., 2021. Astrocytic atrophy as a pathological feature of Parkinson's disease with LRRK2 mutation. NPJ Parkinsons Dis. 7, 31.

Reed, X., et al., 2019. The role of monogenic genes in idiopathic Parkinson's disease. Neurobiol. Dis. 124, 230–239.

Rocha, E.M., et al., 2020. LRRK2 inhibition prevents endolysosomal deficits seen in human Parkinson's disease. Neurobiol. Dis. 134, 104626.

Rodriguez, M., et al., 2007. Bone-marrow-derived cell differentiation into microglia: a study in a progressive mouse model of Parkinson's disease. Neurobiol. Dis. 28, 316–325.

Russo, I., et al., 2015. Leucine-rich repeat kinase 2 positively regulates inflammation and down-regulates NF-kappaB p50 signaling in cultured microglia cells. J. Neuroinflammation 12, 230.

Sanders, L.H., et al., 2014. LRRK2 mutations cause mitochondrial DNA damage in iPSC-derived neural cells from Parkinson's disease patients: reversal by gene correction. Neurobiol. Dis. 62, 381–386.

Sanyal, A., et al., 2020. Lysosome and inflammatory defects in GBA1-mutant astrocytes are normalized by LRRK2 inhibition. Mov. Disord. 35, 760–773.

Satoh, J., et al., 2016. TMEM119 marks a subset of microglia in the human brain. Neuropathology. 36, 39–49.

Schapansky, J., et al., 2018. Familial knockin mutation of LRRK2 causes lysosomal dysfunction and accumulation of endogenous insoluble alpha-synuclein in neurons. Neurobiol. Dis. 111, 26–35.

Schildknecht, S., et al., 2017. Tipping points and endogenous determinants of nigrostriatal degeneration by MPTP. Trends Pharmacol. Sci. 38, 541–555.

Scott, J.D., et al., 2017. Discovery of a 3-(4-Pyrimidinyl) Indazole (MLi-2), an orally available and selective leucine-rich repeat kinase 2 (LRRK2) inhibitor that reduces brain kinase activity. J. Med. Chem. 60, 2983–2992.

Smith, W.W., et al., 2006. Kinase activity of mutant LRRK2 mediates neuronal toxicity. Nat. Neurosci. 9, 1231–1233.

Streubel-Gallasch, L., et al., 2021. Parkinson's disease-associated LRRK2 interferes with astrocyte-mediated alpha-Synuclein clearance. Mol. Neurobiol. 58, 3119–3140.

Teismann, P., et al., 2003. Pathogenic role of glial cells in Parkinson's disease. Mov. Disord. 18, 121–129.

Thirstrup, K., et al., 2017. Selective LRRK2 kinase inhibition reduces phosphorylation of endogenous Rab10 and Rab12 in human peripheral mononuclear blood cells. Sci. Rep. 7, 10300.

Tolosa, E., et al., 2020. LRRK2 in Parkinson disease: challenges of clinical trials. Nat. Rev. Neurol. 16, 97–107.

Tozzi, A., et al., 2018. Dopamine D2 receptor-mediated neuroprotection in a G2019S Lrrk2 genetic model of Parkinson's disease. Cell Death Dis. 9, 204.

Van der Perren, A., et al., 2021. LRRK2 ablation attenuates Alphalpha-Synuclein-induced Neuroinflammation without affecting neurodegeneration or neuropathology in vivo. Neurotherapeutics. 18 (2), 949–961.

Volta, M., Melrose, H., 2017. LRRK2 mouse models: dissecting the behavior, striatal neurochemistry and neurophysiology of PD pathogenesis. Biochem. Soc. Trans. 45, 113–122.

Wallings, R., et al., 2019. LRRK2 interacts with the vacuolar-type H+-ATPase pump a1 subunit to regulate lysosomal function. Hum. Mol. Genet. 28, 2696–2710.

West, A.B., 2017. Achieving neuroprotection with LRRK2 kinase inhibitors in Parkinson disease. Exp. Neurol. 298, 236–245.

West, A.B., et al., 2005. Parkinson's disease-associated mutations in leucine-rich repeat kinase 2 augment kinase activity. Proc. Natl. Acad. Sci. U. S. A. 102, 16842–16847.

West, A.B., et al., 2007. Parkinson's disease-associated mutations in LRRK2 link enhanced GTP-binding and kinase activities to neuronal toxicity. Hum. Mol. Genet. 16, 223–232.

Xiong, Y., et al., 2018. Robust kinase- and age-dependent dopaminergic and norepinephrine neurodegeneration in LRRK2 G2019S transgenic mice. Proc. Natl. Acad. Sci. U. S. A. 115, 1635–1640.

Yao, C., et al., 2010. LRRK2-mediated neurodegeneration and dysfunction of dopaminergic neurons in a Caenorhabditis elegans model of Parkinson's disease. Neurobiol. Dis. 40, 73–81.

Yue, M., et al., 2015. Progressive dopaminergic alterations and mitochondrial abnormalities in LRRK2 G2019S knock-in mice. Neurobiol. Dis. 78, 172–195.

Zhao, H.T., et al., 2017. LRRK2 antisense oligonucleotides ameliorate alpha-Synuclein inclusion formation in a Parkinson's disease mouse model. Mol. Ther. Nucleic Acids 8, 508–519.